Chapter 7
Masonry Piers, Walls, and Towers under Vertical Loads

Abstract. This chapter is addressed to the structural analysis under vertical loads of walls, piers, and towers. For them, the nonlinear interaction between the destabilizing effects of the axial loads and the masonry no-tension response can be very strong. Instability analysis of the masonry pier under an eccentric axial load is firstly studied in the wake of a relevant study of Yokel. The strong sensitivity of the pier strength to the eccentricity of the load is pointed out and comparisons are made with the case of reinforced concrete columns.

Static analysis of building masonry walls is then examined. For them the presence of offsets of the wall thickness at the various stories play a relevant role. Instability of towers whose behavior can be strongly influenced by foundation deformability, is analyzed at the end of the section. Special attention has given to the stability analysis of the Pisa Tower, which recently underwent an outstanding restoration work.

7.1 Introduction

The topic of this chapter is the study of the statics of piers, walls, and towers under vertical dead loads. Owing to their geometry, the behavior of such structures under vertical loads presents specific aspects whose analysis requires assumptions and approaches different from those considered so far. In fact, elastic masonry deformation, which is generally disregarded in arches and vaults because it yields negligible effects on their statics, in masonry piers, and walls instead has important consequences on behavior.

The main aspect of the problem is the nonlinear interactions occurring between any changes in geometry and the no-tension response of the masonry: such interactions lead to high susceptibility of piers and walls to axial load eccentricities – far greater than that of reinforced concrete piers or steel columns to similar actions.

Furthermore, walls under vertical loads exhibit complex behavior, which is moreover strongly dependent on their state of conservation. The connections between walls and floors may in fact degrade over time, in which case, slow lateral deformation of the walls can significantly increase the axial load eccentricities and, consequently, their destabilizing effects. The cracking patterns in walls

M. Como: Statics of Historic Masonry Constructions, SSSSM 1, pp. 401–463.
springerlink.com

can furnish useful information for deciding on the most suitable repair and reinforcement operations to adopt. Similarly, nonlinear stability analysis is also required to study the equilibrium of a tower. Such analyzes, aimed at evaluating any tilting, can in many cases be performed taking into account the deformability of the foundation alone. The basic problem of evaluating the strength of eccentrically loaded piers and walls will be analyzed first in the next sections. Subsequently, many particular aspects of the statics of masonry piers, walls, and towers will be examined and exemplified through some important case studies.

7.2 Piers

7.2.1 Strength of Masonry Piers under Eccentric Axial Loads: Mechanical Aspects of the Problem

Eccentrically loaded masonry piers behave very differently from reinforced concrete columns. A regular series of cracks occurs in reinforced concrete piers, and the concrete between adjacent cracks bears the tensile stresses: this effect, usually called *tension stiffening*, attenuates the nonlinear response of the column.

In masonry piers, on the contrary, cracking spreads diffusely throughout wide areas of the structure, and the nonlinear effects are much more severe: they strongly reduce the pier's strength. Even small eccentricities of the axial loads can produce serious reductions in strength.

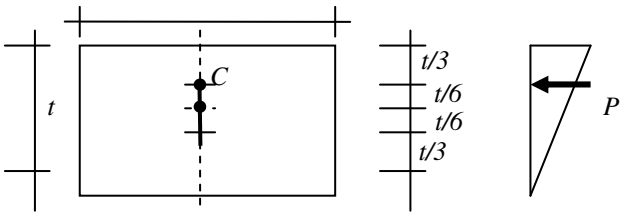

Fig. 7.1. Rectangular section with the positions of its core edge. The stress distribution corresponds to an eccentricity equal to half the core width

In the stability analysis of masonry piers it is usually assumed that the elastic strains vary linearly with distance from the neutral axis across the sections of the piers, if eccentrically loaded. The eccentricity e of the axial load P measures the distance of the point load, i.e. point C of application of load P, from the center of the section. The distance of point load C from the compressed edge of the section is indicated by u. For the sake of simplicity, we shall refer to rectangular pier cross-sections. The section is wholly compressed (fig. 7.1) only when the point load is included within the core of the section, i.e. when the eccentricity e of P falls within the interval

$$-t / 6 \le e \le t / 6 \ . \tag{1}$$

This is the case of *low eccentricities*.

In figure 7.1 the point load *C* is located at the edge of the core, i.e. $e = t/6$. In this case, the neutral axis skirts the lower edge of the section: the stresses exhibit the triangular distribution shown in the figure. For the rectangular section we know that the core width equals $t/3$. Thus, with t the height of the section, the above-defined distance u is equal to $t/3$. Elastic flexural deformations must be taken into account in the analysis of an eccentrically loaded pier. Such deformations increase the axial load eccentricity and narrow the resistant areas of the pier sections (fig. 7.2).

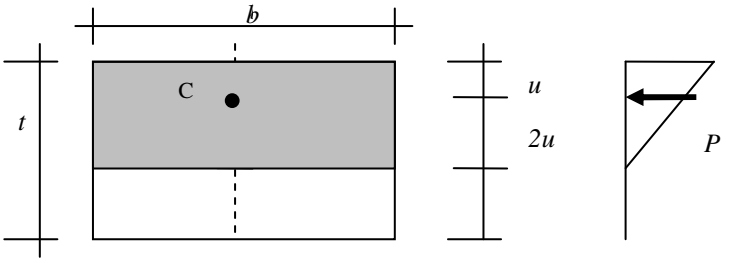

Fig. 7.2. The narrowed resistant section under a strongly eccentric axial load

With gradually increasing axial load intensity, this effect becomes more and more relevant and the pier may collapse. Figure 7.3 shows the effect of the flexural deformation and the crack distribution in a masonry pier of height *h,* with transverse rectangular sections of dimensions $b \cdot t$, eccentrically loaded at its end sections..

The hatched area in figure 7.3 indicates the resisting region of the pier and highlights the effect of the elastic bending deformations. Note that the extension of the cracked region would result to be greatly reduced if these bending deformations were neglected. Such an evaluation of the strength of piers taking into account its flexural deformations was first performed by Yokel (1971). This analysis refers to the pier's *compressed edge*. It is in fact simpler to refer to this edge, rather than to the pier central axis, which continuously changes position inside the resistant sections during loading.

The end sections of the pier are assumed to be hinged. The constraining effects of floors present at the head and base of piers or building walls, as well as the presence of flying buttresses and buttresses in cathedrals piers, justify this assumption.

7.2.2 Differential Equation of the Inflexion of an Eccentrically Loaded Cracked Pier

In this analysis, the reference parameter is the distance u between the compressed edge and the axis of load *P:* owing to the lateral inflexion, this distance varies

along the height of the pier. The axial load P is applied at its end sections with eccentricity e falling within the interval $t/2 > e \geq t/6$, where t is the section width.

In figure 7.3 the distance of the axial load P from the generic edge of the pier section is indicated by u, while u_1 and u_o are the same distances but to the end and the mid-section of the pier, respectively. We thus have $u_1 = t/2 - e$. This *strong eccentricity* condition loading corresponds to positions of the point load of P at the pier end sections included between the edges of the section and its core. The axial load narrows *all* the resistant sections of the pier. (The case of *low eccentricities*, i.e. corresponding to eccentricities e included within the section core, with $t/6 \geq e \geq 0$, will be considered later.) Returning to the strong eccentricities, we must now evaluate the changes in the resistant sections' areas along the height of the pier due to its inflexion.

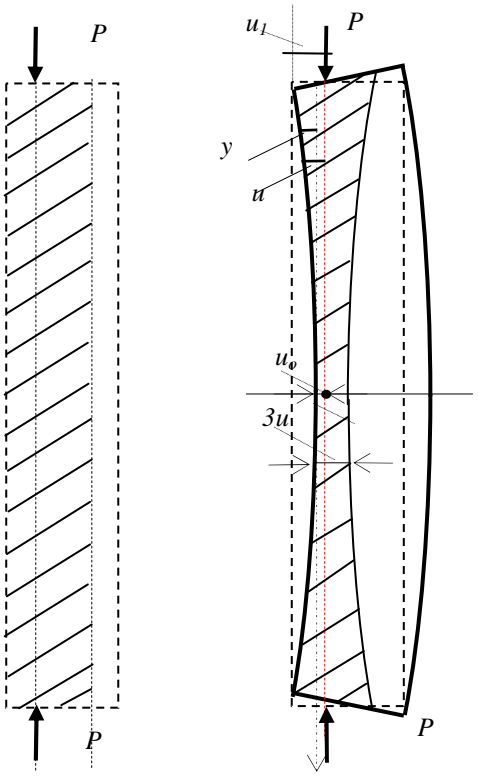

Fig. 7.3. Dramatic narrowing effect of the pier resistant zone due to flexural deformations

The straight line defining the direction of load P, represented by a dotted line in figure 7.3, passes at distance u from the compressed edge at any section of the pier. As shown in the figure, distance u gradually decreases from the end to the mid-section: the maximum distance u_1 is reached at the end sections of the pier,

the minimum u_0 at the mid-section. The stresses have a *triangular distribution* at each transverse section of the pier: compression vanishes at the crack tip. On the opposite side, the compression is

$$\sigma_o(u) = \frac{2P}{3bu} \ , \tag{2}$$

where $\sigma_0(u)$ is the *local* maximum stress in the section whose compressed edge is at distance u from the P axis.

The maximum compression stress of all the local maximum stresses $\sigma_0(u)$, indicated by σ_{max}, occurs at the pier mid-section, at distance $h/2$ from the end sections and equals:

$$\sigma_{\max} = \frac{2P}{3bu_0} \ . \tag{3}$$

Figure 7.4, shows the deformation of the pier's compressed edge: the origin of the reference axes is at the mid-section. Axis x is parallel to the direction of P and tangential to the deformed compressed edge at the origin O. Now let y be the distance between the line of the pier's compressed edges from axis x. Thus, at each section of the pier, we have

$$y = u - u_0 \tag{4}$$

and, for $x = h/2$, $y = u_1 - u_o$. Figure 7.5 shows a small element of the pier between the external edge and the boundary of the cracked zone. The distance between the unloaded and the compressed edges of the element equals $3u$. The length of the element, from the unloaded side, is dl, whereas the length of the compressed edge is $dl - \varepsilon dl$, with ε the strain in the external compressed edge of the element. A relative rotation ϕ occurs between the side sections of this element, as shown in figure 7.5.

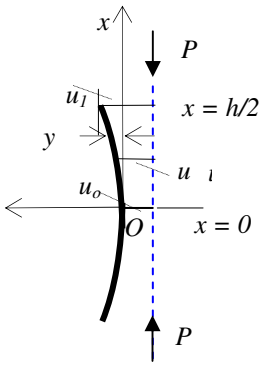

Fig. 7.4. Inflexion curve of the compressed edge with reference axes *xy*

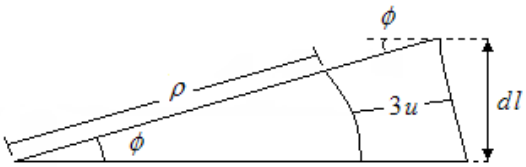

Fig. 7.5. Curvature of the compressed edge.

This rotation ϕ can be obtained as

$$\phi = \frac{\varepsilon \cdot dl}{3u} \quad . \tag{5}$$

The strain ε in the external compressed edge, on the other hand, can be evaluated according to (2), as

$$\varepsilon = \frac{\sigma_o}{E} = \frac{2P}{3bu}\frac{1}{E} \quad , \tag{6}$$

where E is the elastic modulus of the masonry. Thus, taking (6) into account, the relative rotation ϕ becomes

$$\varphi = \frac{\varepsilon \cdot dl}{3u} = \frac{2P}{9Eb}\frac{dl}{u^2} \quad . \tag{5'}$$

The length of the compressed side of the element, equal to $dl(1-\varepsilon)$, can be expressed in terms of the radius of curvature ρ of the curved compressed edge as

$$\rho\varphi = dl \cdot (1-\varepsilon) \tag{7}$$

and

$$\frac{1}{\rho} = \frac{\phi}{dl \cdot (1-\varepsilon)} = \frac{2P}{9Eb} \cdot \frac{1}{u^2 \cdot (1-\varepsilon)} \quad . \tag{8}$$

The curvature of the function

$$y = y(x) = u(x) - u_o \tag{9}$$

is, as a rule, given by

$$\frac{1}{\rho} = \frac{\phi}{dl \cdot (1-\varepsilon)} = \frac{2P}{9Eb} \cdot \frac{1}{u^2 \cdot (1-\varepsilon)} \ , \tag{10}$$

whence

$$\frac{d^2y}{dx^2} = \frac{1}{\rho} \cdot [1 + (\frac{dy}{dx})^2]^{3/2} = \frac{2P}{9Eb} \cdot \frac{[1 + (\frac{dy}{dx})^2]^{3/2}}{u^2 \cdot (1-\varepsilon)} \ . \tag{11}$$

Strains ε are small quantities ($\varepsilon < 0.005$) and dy/dx is thus negligible with respect to unity; so all in all we can assume

$$\frac{[1 + (\frac{dy}{dx})^2]^{3/2}}{1-\varepsilon} \approx 1 \ . \tag{12}$$

The second derivative d^2y/dx^2, which represents the curvature of the compressed pier edge, is

$$-\frac{d^2y}{dx^2} = \frac{2P}{9Eb} \cdot \frac{1}{u^2} \ . \tag{13}$$

The factor $2P/(9Eb)$ is constant along x, so we can write

$$k_1 = \frac{2P}{9Eb} \ . \tag{14}$$

On the other hand, according to (9), we have

$$u = u_0 + y \tag{9'}$$

and the differential equation for the flexure of the eccentrically loaded cracked pier becomes

$$\frac{d^2y}{dx^2} = \frac{k_1}{(u_o + y)^2} \tag{15}$$

The following boundary conditions are associated to equation (15):

– at $x = h/2$, i.e. at the pier head, $y = u_1 - u_o$; (16)

– at $x = 0$, i.e. at the mid-section, $y = 0$. (16')

Integration of (15), satisfying the above boundary conditions (see Appendix), yields

$$P = \frac{9Ebu_1^3}{h^2} \cdot \alpha \cdot [\sqrt{1-\alpha} + \alpha \ln(\sqrt{\frac{1-\alpha}{\alpha}} + \sqrt{\frac{1}{\alpha}})]^2 \ , \tag{17}$$

where

$$\alpha = u_0 / u_1 \ . \tag{18}$$

Note that the eccentricity e is given by

$$e = \frac{t}{2} - u_1 \ . \tag{19}$$

Equation (17) expresses the relation between the flexure factor α and the eccentric axial load P.

7.2.3 Collapse Load

Let us now define a reference critical load

$$P_{eq} = \frac{\pi^2 EI_e}{h^2} \ , \tag{20}$$

which is evaluated by means of the moment of inertia I_e of the resistant section at the pier head; this section has height $3u_1$. The moment of inertia I_e is thus given by

$$I_e = \frac{27bu_1^3}{12} \ . \tag{21}$$

In particular, when the point load at the head section is located at the edge of the core section, i.e. with $3u_1 = t$, the entire section is resistant and load P_{eq} matches the Euler load P_E. In fact, we obtain

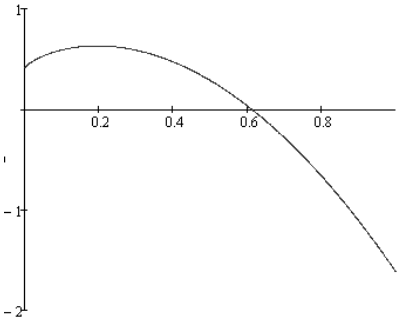

Fig. 7.6. The derivative of the function P/P_{eq} with respect to the variable a

$$P_{eq}\left(3u_1 = t\right) = \left(\frac{\pi^2 E}{h^2} 27 \frac{b u_1^3}{12}\right)_{u_1 = t/3} = \frac{\pi^2 EI}{h^2} = P_E \ , \tag{22}$$

where

$$I = \frac{bt^3}{12} \ . \tag{23}$$

Taking (20) and (21) into account, condition (17) becomes:

$$\frac{P}{P_{eq}} = \frac{4}{\pi^2} \cdot \alpha[\sqrt{1-\alpha} + \alpha \ln(\sqrt{\frac{1-\alpha}{\alpha}} + \sqrt{\frac{1}{\alpha}})]^2 \ . \tag{24}$$

Equation (24) holds for $t/2 > e \geq t/6$, where e is the load eccentricity at the end pier sections. Condition (24), first determined by Yokel, expresses the dependence of the applied eccentric axial load P on the pier inflexion at its mid-section. The derivative of the function P/P_{eq} with respect to variable a is sketched out in figure 7.6. This derivative vanishes for

$$\alpha = \alpha = \bar{\alpha} = 0.6116 \ . \tag{25}$$

Function P/P_{eq} attains a maximum for $\alpha = \bar{\alpha} = 0.6116$. The flexure parameter α thus equals unity when the pier is not inflexed, i.e. for $P = 0$. With increasing P, the pier starts to bend and parameter u_o decreases, as does factor α. Figure 7.7 gives a dimensionless representation of function (24) by assuming eccentricity $e = t/6$.

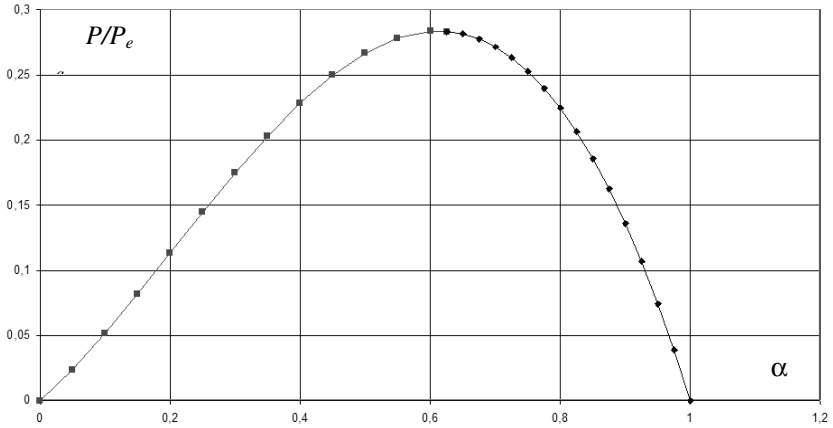

Fig. 7.7. Equilibrium states of the masonry pier loaded with eccentricity: $e = t/6$

The point with coordinates ($\alpha = u_o/u_1$=1, $P/P_{eq} = 0$) represents the rectilinear configuration of the pier when the axial load is zero. On the contrary, the point with coordinates ($\alpha = u_o/u_1 = 0$, $P/P_{eq} = 0$) corresponds to a state of cracking so widespread as to produce an internal hinge in the pier and, consequently, vanishing of the axial load intensity strength, as shown in figure 7.8. In this case, equilibrium in the pier under zero axial load can be maintained only with $u_o/u_1 = 0$.

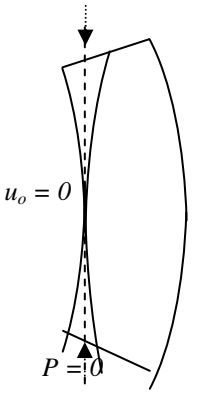

Fig. 7.8. The pier at the state $P = 0$, $u_o = 0$

Using (19) we can trace the entire pier equilibrium path with gradually increasing P and the given eccentricity defined by parameter u_1. The equilibrium path runs from right to left along the diagram in figure 7.7. Initially, starting at $P = 0$,

load P increases, while bending factor $\alpha = u_o/u_1$ decreases. The first branch of the equilibrium states describes this behavior for α varying from $\alpha = 1$ to $\alpha = 0.6115$, just where P attains its maximum. All the points belonging to this branch represent stable equilibrium states. At the point defined by $\alpha = 0.6115$, the axial load equals $P/P_{eq} = 0.285$, which is the maximum load that the pier can sustain: any further increment of P will now lead to collapse of the pier by *loss of equilibrium.*

In conclusion, collapse of the pier loaded axially with high eccentricity e, i.e. with $t/2 > e \geq t/6$, will come about under the axial load

$$P_{cr} = 0.285 \frac{I_e}{I} P_E \ , \tag{26}$$

where, according to (21), the eccentricity e is present in the expression for I_e, the moment of inertia of the resistant section at the pier head. Alternatively, highlighting the dependence of the critical load on the eccentricity e at the end sections of the pier, from (26) we have

$$\frac{P_{cr}}{P_E} = 0.285\left(\frac{3}{2} - \frac{3e}{t}\right)^3 \qquad t/2 > e \geq t/6 \ . \tag{26'}$$

In particular, from (26'), when the eccentricity e equals $t/6$, i.e. when the load is applied at the core edge of the end sections, we obtain $P_{cr}/P_E = 0.285$. For larger eccentricities the reduction in the critical load with respect to the Euler load is greater. For $e = t/2$ the critical load vanishes altogether.

The values of P/P_{eq} corresponding to the descending branch of the curve in figure 7.7, i.e. to values of α within the interval $0.625 > \alpha > 0$, have limited physical significance: they correspond to the pier inflexion that can be maintained with a load below the critical one. They are all unstable equilibrium states.

7.2.4 Pier Compression Strength with Varying Load Eccentricity

The foregoing results have been generalized by Frisch–Fay (1975) and De Falco A. and Lucchesi M. (2000, 2003) to consider the entire variability range of eccentricity. Figure 7.9 shows the collapse load of the pier versus the ratio e_L/d, in dimensionless form, where e_L is the eccentricity and $d = t$ the section height, considering both weak and strong eccentricities. When the eccentricity vanishes, that is, when the ratio e_L/d is nearly 1/1000, the collapse load matches the Euler load P_E given by (22). As the eccentricity increases, the pier compression strength decreases: for $e_L/d = 1/10$ the pier strength is about 70% of the Euler load, while the pier strength equals the above-cited strength of $0.285P_E$ when e_L/d reaches the value 1/6.

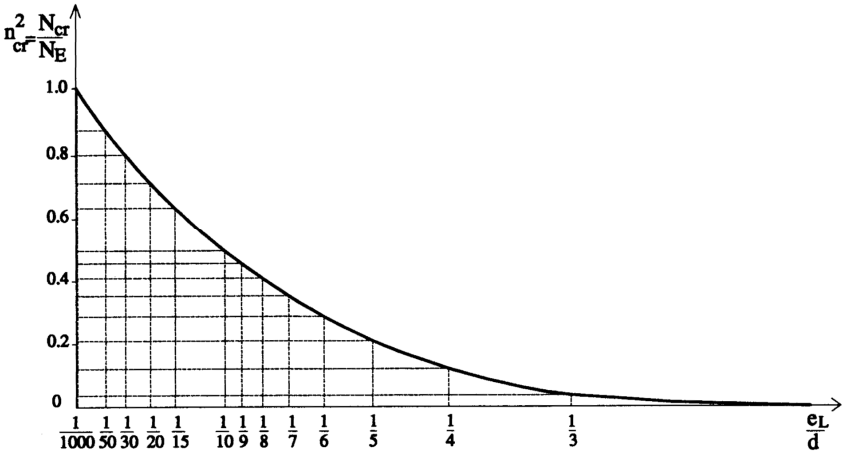

Fig. 7.9. Dimensionless strength P_{cr}/P_E of a masonry pier loaded eccentrically by varying the eccentricity factor e_L/d (De Falco, Lucchesi, 2003)

7.2.5 Influence of the Pier Weight

The pier weight is represented by a series of uniformly distributed loads, *w*, equivalent, overall, to the total weight *W*, assumed to be nonnegligible with respect to *P*. The combined action of load *P,* applied at the pier head, and distributed loads *w* is a significant and likely loading condition, frequent, for instance in the high piers of a cathedral.

Figure 7.10 shows a pier of height 2*L,* hinged at its end sections, loaded by the force *P* at its head and by the distributed weight *w*. This case is also equivalent to that of a cantilever pier of height *L* under equal loads. Figure 7.11 shows the results obtained by L. La Mendola and M. Papia (1993).

The ordinates represent the dimensionless values of the maximum head load that the pier can sustain with the assumed ratio *W/P* and eccentricity ratio *e/H*, where *H* indicates the pier section height. Inspection of the diagrams in figure 7.11 reveals that the addition of weight *W*, *if relevant with respect to P,* in the presence of *large eccentricities*, increases the load *P* that the pier can sustain. In this case, we say that the weight *W* has a stabilizing effect.

To the contrary, in the presence of *small eccentricities*, the effect of the weight has, as a rule, a destabilizing effect. Other load combinations have been considered, in particular, the case of a concurrent shear force together with an axial load applied at the pier head (Como, Ianniruberto, 1995).

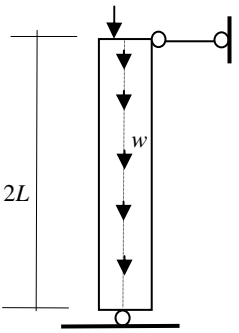

Fig. 7.10. Pier loaded both by an eccentric force at its head and its own weight distributed along its length

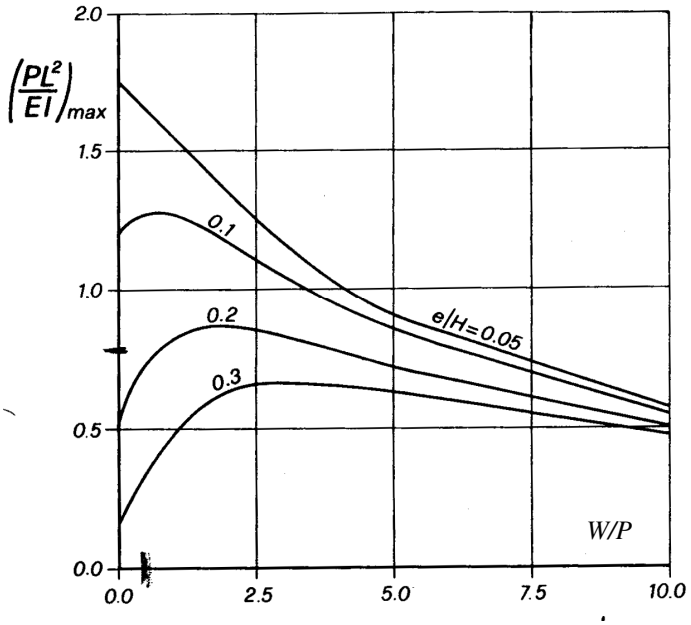

Fig. 7.11. Stabilizing or destabilizing effects of weight *W* on the magnitude of the head load *P* that a pier can sustain (da La Mendola, Papia 1993)

7.2.6 The Use of Nonlinear Programs in the Stability Analysis of Masonry Piers

The use of nonlinear programs, such as ATENA (Cervenka, 2002) or DIANA (Frits and Wijtze, 1990), able to account for both material and geometrical nonlinearities, can be very useful for analyzing the static behavior of masonry piers

with more complex geometry and load distributions. Both these programs assume low tensile strength, as in the $\sigma - \varepsilon$ diagram shown in figure 7.12.

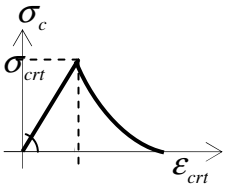

Fig. 7.12. Tensile $\sigma - \varepsilon$ diagram assumed in the nonlinear programs

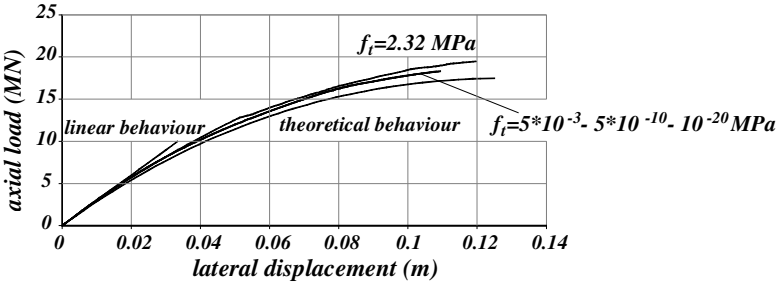

Fig. 7.13. Axial load-lateral displacement diagrams for eccentricity $e = L/6 = 16.7$ cm

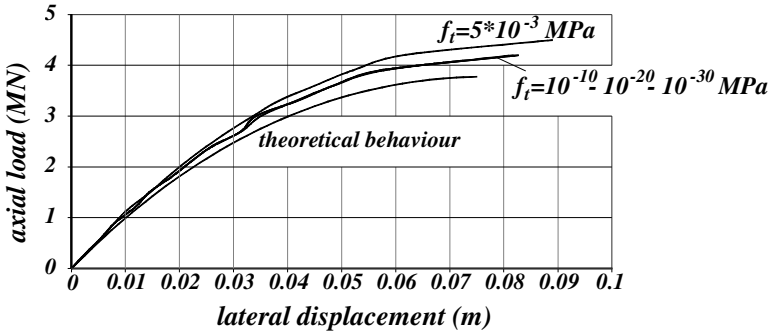

Fig. 7.14. Axial load – lateral displacement diagrams for $e = 30$ cm

The first example presented in the following can highlight the ability of these programs to accurately describe the behavior of masonry piers under eccentric loads. The example considers a pier of constant section loaded at its head by an eccentric load. The numerical results can thus be compared with those from

equation (24). The pier has a square section with side length L = 1 m and height H = 10 m. The stress-strain diagram is of the type shown in figure 7.13, and discussed in Chapter I. The program considers nonzero tensile strength that can be suitably reduced in the calculations.

The assumed elastic constants for the masonry are: elastic modulus, 3.032 E + 04 *MPa*; Poisson coefficient, ν = 0; tensile strength, 5 E – 03 *MPa*; and compression strength, 2.5 E + 05 *MPa*. The example addresses two different eccentricities: $e_1 = L/6 = 16.7cm$ and $e_3 = 30cm$. The value of the head axial load, assumed initially $P = 3 \cdot 10^{-1}\, MN$, increases gradually. Collapse comes about when the tangent becomes horizontal on the axial load – lateral displacement diagram, as shown in figures 7. 13 and 7.14. The corresponding collapse loads turn out to be only slightly higher than the collapse loads resulting from application of Eq. (24).

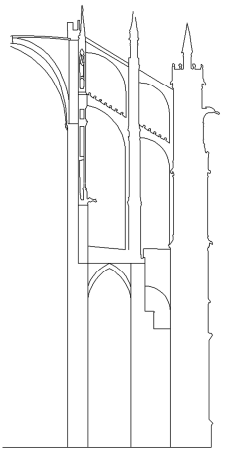

Fig. 7.15. Piers of a Gothic cathedral

7.2.7 Effects of Mortar Creep on the Behavior of an Eccentrically Loaded Pier

7.2.7.1 Simplified Model of a Visco-Elastic No-Tension Pier

The creep of mortars, examined in Chapter I, can significantly, albeit slowly, increases the destabilizing effects of axial load on masonry piers or walls. Thorough study of the problem can be performed by modifying the previously examined Yokel formulation in order to account for the creep deformation of mortar, examined in Section 1.13.2.1. Such an approach is, however, very complex and only some simplified solutions to the problem can be obtained in practice. One simplified creep model of an eccentrically loaded, elastic no-tension pier considers the presence of a single central viscous, no-tension voussoir, as shown in figure 7.16.

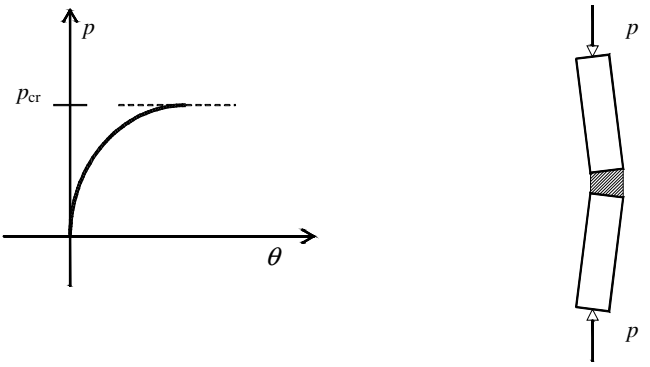

Fig. 7.16. Simplified creep model of an elastic no-tension pier

A load P is applied with eccentricity e with respect to the center G of the section at height h from its base of width L (fig. 7.17). The pier rotates by a small angle θ under the action of the eccentric axial load P.

Owing to pier rotation θ, the eccentricity of P becomes $(e + h\theta)$. The distance u of the axis of P from the external edge of the base section is thus

$$u = (L/2 - e - h\theta) \,. \tag{27}$$

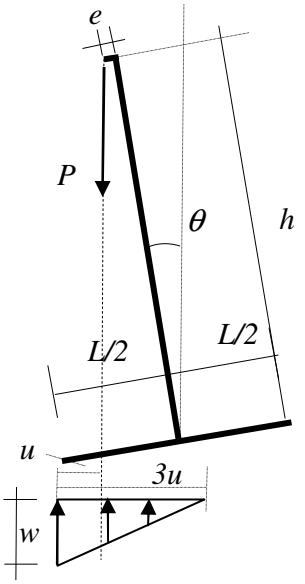

Fig. 7.17. Geometrical and mechanical quantities defining the central viscous no-tension voussoir

We can assume that *only* the central voussoir exhibits elastic no-tension behavior. Thus, the equilibrium equation of the inclined pier, in the case of small eccentricity, i.e. with $(e + h\theta) < L/6$, is

$$p = \frac{9}{2}(\gamma - \theta)^2 \theta \ , \tag{28}$$

where

$$p = \frac{P}{Eh^2} \qquad \gamma = \frac{L}{2h} - \frac{e}{h} \ . \tag{29}$$

The critical state is thus reached when

$$\frac{dp}{d\theta} = -\frac{9}{2} 2(\gamma - \theta)\theta + \frac{9}{2}(\gamma - \theta)^2 = 0 \, , \tag{30}$$

i.e. when the critical rotation

$$\theta_{cr} = \frac{\gamma}{3} \tag{31}$$

is attained. The dimensionless elastic critical load is therefore

$$p_{cr} = \frac{2}{3}\gamma^3 \ . \tag{32}$$

Creep deformation of the central voussoir gradually increases the rotation of the pier. By using the memory function considered in Section 1.13.2.1, in place of (30), we obtain the following equation governing the evolution of the pier equilibrium state over time:

$$3u(t)\theta(t) = \lambda\varepsilon_{tot}(t) = \lambda[\frac{2P}{3bEu(t)} + \alpha\beta\int_{t_1}^{t} e^{-\beta(\tau - t_o)} \frac{2P}{3bEu(\tau)} d\tau] \ . \tag{33}$$

Substituting the expression for distance, $u(t)$, into Eq. (33) gives the relation between the rotation $\theta(t)$ and the dimensionless eccentric load p

$$\xi = 1 - \frac{9}{2}\frac{1}{\alpha p}[\gamma^2(\theta - \theta_o) - 3/2\gamma(\theta^2 - \theta_o^2) + 2/3(\theta^3 - \theta_o^3)] - \frac{1}{\alpha}\ln\frac{(\gamma - \theta)}{(\gamma - \theta_0)} \, , \tag{34}$$

where the variable ξ is

$$\xi = e^{-\beta t} \ , \tag{35}$$

and where for the sake of simplicity we have assumed $t_o = t_1 = 0$. In Eq. (34), θ_o and $\theta(t)$ respectively indicate the initial and generic rotations, i.e., the rotations occurring at the initial time $t = 0$ and at time t. The asymptotic pier rotation, for $t \to \infty$, i.e., when $\xi \to 0$, is indicated by θ_∞, hence, from Eq. (34), with $\xi = 0$ we obtain

$$0 = 1 - \frac{1}{\alpha}\frac{9}{2p}[\gamma^2(\theta_\infty - \theta_o) - 3/2\gamma(\theta_\infty^2 - \theta_o^2) + 2/3(\theta_\infty^3 - \theta_o^3)] - \frac{1}{\alpha}\ln\frac{(\gamma - \theta_\infty)}{(\gamma - \theta_0)} \ . \tag{34'}$$

Thus, Eq. (34') furnishes the asymptotic rotation θ_∞ produced by load P.

7.2.7.2 The Critical State: Comparison with the Simplified Solution Obtained via the Delayed Modulus Approach

The critical state of the pier is reached when

$$\frac{d\xi}{d\theta} = 0 \ . \tag{36}$$

Condition (36) defines the presence of *simultaneous* equilibrium states at the same time t. From (36) and by using (34), we obtain

$$-2\theta_{cr}^3 + 5\gamma\theta_{cr}^2 - 4\gamma^2\theta_{cr} + (\gamma^3 - \frac{2}{9}p_{cr}) = 0 \ . \tag{37}$$

The critical state is attained at $t \to \infty$ if both the rotation $\theta = \theta_{cr\infty}$ and load $p_{cr\infty}$ satisfy the equation

$$-2\theta_{cr,\infty}^3 + 5\gamma\theta_{cr,\infty}^2 - 4\gamma^2\theta_{cr,\infty} + (\gamma^3 - \frac{2}{9}p_{cr,\infty}) = 0 \tag{37'}$$

as well as Eq. (34'), i.e.,

$$0 = 1 - \frac{1}{\alpha}\frac{9}{2p_{cr,\infty}}[\gamma^2(\theta_{cr,\infty} - \theta_o) - 3/2\gamma(\theta_{cr,\infty}^2 - \theta_o^2) + 2/3(\theta_{cr,\infty}^3 - \theta_o^3)] - \frac{1}{\alpha}\ln\frac{(\gamma - \theta_{cr,\infty})}{(\gamma - \theta_0)} \ . \tag{34''}$$

The quantities $\theta_{cr\infty}$ and p_{cr} in Eq. (37')$_\infty$ are unknowns, while the unknowns in Eq. (34") are $\theta_{cr\infty}$,θ_o, and $p_{cr\infty}$. The last equation required for the solution is obtained from Eq. (30), which gives the rotation θ_o at initial time $t = 0$ under load $p_{cr\infty}$, which yields

$$\frac{2}{9} p_{cr,\infty} = (\gamma - \theta_o)^2 \theta_o \,. \tag{30'}$$

Substitution of (30') into (37') and (34") yields

$$x(1-3/2x+2/3x^2) - x_o(1-3/2x_o+2/3x_o^2) = x_o(1-x_o)^2[\alpha + \ln\frac{(1-x_0)}{(1-x)}] \tag{38}$$

$$(1-x_o)^2 x_o = -2x^3 + 5x^2 - 4x + 1 \,, \tag{39}$$

where

$$x_o = \theta_o / \gamma \qquad x = \theta_{cr,\infty} / \gamma \,. \tag{40}$$

Solution of Eqs. (38) and (39) for assigned values of the creep factor α furnishes the values $\theta_{cr\infty}$ and θ_o. The asymptotic critical load $p_{cr\infty}$ is thus obtained by substituting the expression for θ_o into (30').

Table 7.1 reports the values of x and x_o obtained by solution of Eqs. (38) and (39) for the assumed values of creep factor α. Table 7.2 shows the values of the asymptotic rotation $\theta_{cr\infty}$ and the initial rotation θ_o, together with the dimensionless asymptotic critical load and $p_{cr\infty}$ associated with the above solutions for x and x_o.

Table 7.1. Solutions of Eqs. (38) and (39) according to the assumed values of creep factor α

α = 0	x_o = 1/3	x = 1/3
α = 1	x_o = 0.102	x = 0.390
α = 2	x_o = 0.067	x = 0.415
α = 3	x_o = 0.050	x = 0.430
α = 4	x_o = 0.040	x = 0.441

The asymptotic critical loads and $p_{cr,\infty,del}$ have also been obtained by direct substitution of the delayed elastic modulus

$$E_\infty = \frac{E}{1+\alpha} \tag{41}$$

into the elastic no-tension solution (30).

Table 7.2. Asymptotic critical loads according to the assumed values of creep factor α

α =1	$\theta_{cr,\infty} = 0.390\gamma$	$\theta_o = 0.102\gamma$	$p_{cr,\infty} = 0.370\gamma^3$	$p_{cr,\infty,del} = 0.335\gamma^3$
α=2	$\theta_{cr,\infty} = 0.415\gamma$	$\theta_o = 0.067\gamma$	$p_{cr,\infty} = 0.262\gamma^3$	$p_{cr,\infty,del} = 0.222\gamma^3$
α=3	$\theta_{cr,\infty} = 0.430\gamma$	$\theta_o = 0.050\gamma$	$p_{cr,\infty} = 0.203\gamma^3$	$p_{cr,\infty,del} = 0.167\gamma^3$
α= 4	$\theta_{cr,\infty} = 0.441\gamma$	$\theta_o = 0.040\gamma$	$p_{cr,\infty} = 0.166\gamma^3$	$p_{cr,\infty,del} = 0.133\gamma^3$

The critical loads have thus been obtained as

$$p_{cr} = \frac{1}{1+\alpha}\frac{2}{3}\gamma^3 \ . \tag{42}$$

These values are also reported in the last column of Table 6.2. The elastic modulus (41) defines the ratio

$$E_\infty = \frac{\sigma}{\varepsilon_{tot,\infty}} \tag{43}$$

between the acting stress, which is constant over time, and the asymptotic total strain $\varepsilon_{tot,\infty} = \varepsilon_{el} + \varepsilon_{visc\infty}$, which is the sum of the elastic and asymptotic viscous strain. The delayed critical asymptotic loads $p_{cr,\infty\ del}$ are *approximate* solutions to the problem of the critical load evaluation of the no-tension creep model of a pier. Although these approximate values $p_{cr,\infty\ del}$ are consistently lower than the corresponding exact values $p_{cr,\infty}$, they also approximate them quite closely, as is evident in the last two columns of Table 7.2. This outcome highlights that, despite the complexity of the problem, the simplified critical loads obtained using the delayed elastic modulus can represent the actual critical loads with sufficient approximation. The collapse of the Beauvais cathedral in 1294 will be taken up in the Chapter VIII as an example application of the delayed modulus approach to creep buckling.

7.3 Building Walls

7.3.1 Introduction

Figure 7.18 shows the plan of a masonry building with different arrays of longitudinal and transverse walls. Figure 7.19 shows a section of another common historic building, from foundation to roof. The walls present offsets along the vertical due to the varying wall thickness along the height – an arrangement which

is justified by the considerably greater axial loads on the floor levels (Figs. 7.20 and 7.21). While the offsets on the internal walls are symmetrical, those on the external walls were generally made only on the inner side, in order to give buildings smooth vertical facades. Offsets were moreover frequently used as supports for floors.

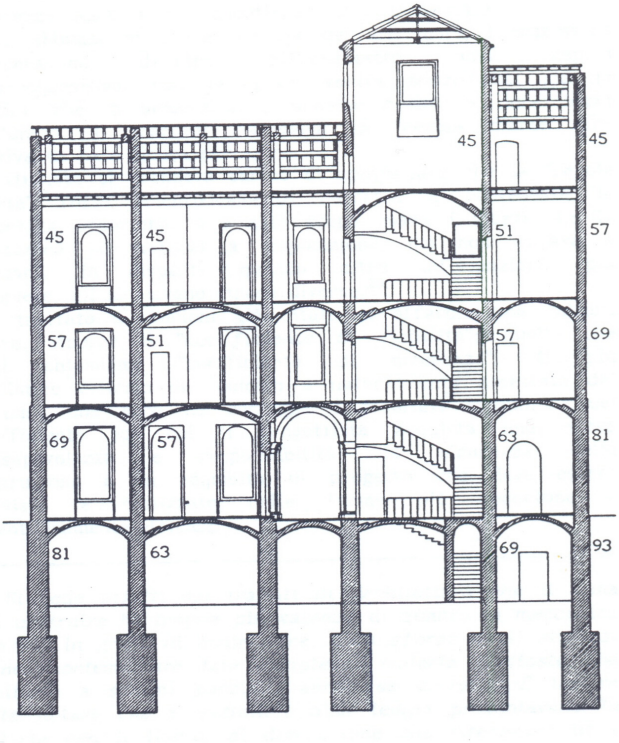

Fig. 7.18. Section of an historic masonry building (Giuffrè A., 1990)

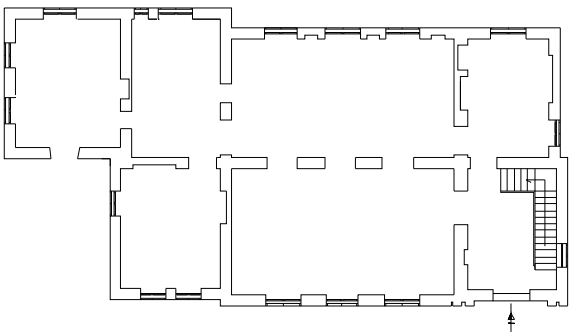

Fig. 7.19. Plan of an historic masonry building

In modern masonry buildings, ring beams running atop the walls at each floor efficiently oppose the transverse flexure of the facade walls and represent stiff transverse constraints on the walls. Historic and older buildings, to the contrary, lack such ring beams.

Only a weak connection is offered at the floor levels by the friction between the floor's steel or wooden beams in contact with the walls at their supports. The connections between the different walls may thus be quite precarious. Particularly at corners, the connections between the stones or bricks may be degraded and even lacking, despite interpenetration between them at the wall intersections. The walls of old buildings are often visibly damaged, and studying the cracking patterns can furnish useful information about the causes of such damage.

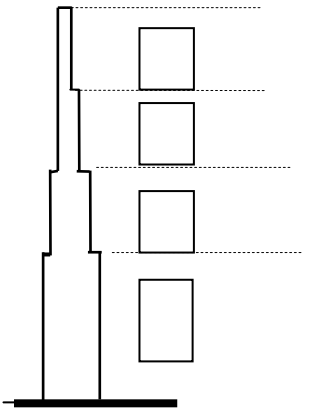

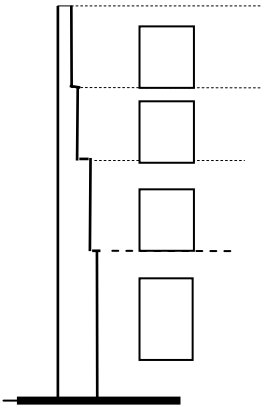

Figs. 7.20 and 7.21. Sections of inner (left) and outer (right) walls with symmetrical and asymmetrical offsets due to varying thickness along the height

7.3.2. Damage and Frequent Cracking Patterns in Old Buildings under Vertical Loads

Vertical loads clearly represent the most significant and long-lasting actions on historic buildings: the weight acts constantly and is responsible for most of the damage occurring in such buildings.

Due to their varying thickness along the height, the external walls are subjected to eccentric axial forces, and present a latent tendency to bulge outwards (Figs. 7.22 and 7.23). In historic buildings this tendency is opposed only by the connections between the different constituent walls, which may be more or less efficient. Moreover, these connections may be weakened by the presence of openings near the wall intersections or by cracking. Sometimes, chains were used to firmly connect the different arrays of walls. Figure 7.24 shows a typical cracking pattern in a transverse wall, near the joint to the facade, caused by rotation around the toe of the facade wall.

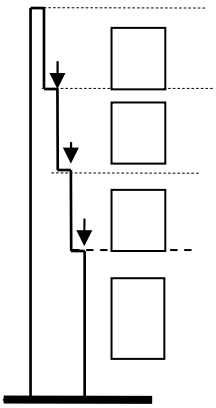

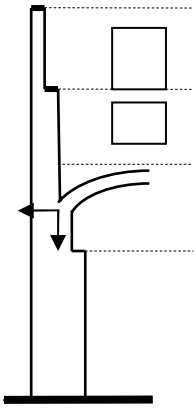

Figs. 7.22 and 7.23. Facade walls. Opposing and concurring actions of floor loads, wall weights, and vault thrusts

Cracks develop on the band of masonry overlying an opening and of course vertically upward, increasing in width as they spread. Such cracks are due to the horizontal tensile stresses occurring in this band due to the outward rotation of the wall. In some cases horizontal cracks may also appear in the floors near their connections to the façade wall.

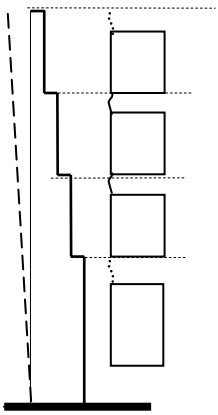

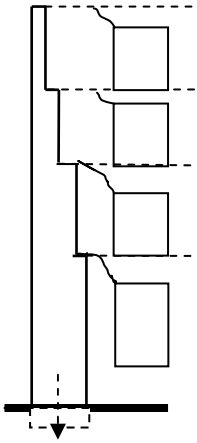

Figs. 7.24 and 7.25. Detachment cracks due to rotation (left) or subsidence (right) of a facade wall

Figure 7.26 shows the cracking pattern in the transverse wall from subsidence of the facade. Typically, such cracks are inclined by about 45° from the vertical and are caused by subsidence of the façade wall, which produces shear stresses on the masonry band overlying the opening in the transverse wall (fig. 7.26).

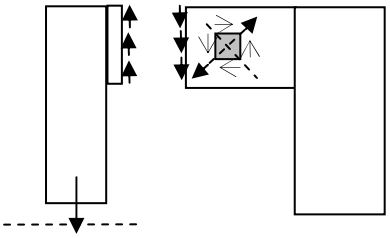

Fig. 7.26. Wall cracks above an opening due to subsidence of the facade wall

Figures 7.27 and 7.28 show analogous situations in the façades of buildings whose interior transverse walls have subsided. When the connection is weakened or lost, the external walls can undergo outward flexions and strong out-of-plumb rotations. The main aim of any restoration work is to reestablish firm connections between the disjointed walls.

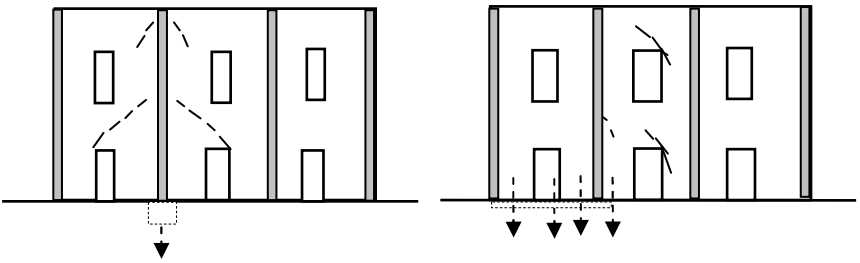

Figs. 7.27 and 7.28 Facade wall cracks due to subsidence of transverse walls

7.3.3 Stresses Due to Vertical Loads

7.3.3.1 Weak Diffusion of Point Loads in Walls

Only two bricks of the lowermost course are engaged – numbers 8 and 9 –, as illustrated in figure 7.29. Any lower course would again exhibit only two blocks engaged, and so on.

A necessary preliminary operation for checking the safety of a building is to perform an evaluation of the compression stresses acting on the walls. The bases of bricks 2 and 3 (in the second course from the top) are only partially

compressed, but they, in turn, engage the underlying three bricks very differently. The two outer blocks, 4 and 6, are in fact subjected to strong eccentric compression.

The weak load diffusion described in Chapter II within the no-tension framework is thus also confirmed by regarding the wall as composed of bricks and weak mortar beds (fig. 7.30).

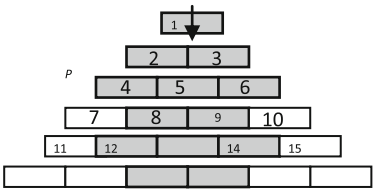

Fig. 7.29. Transmission of vertical load *P* across various courses of a wall

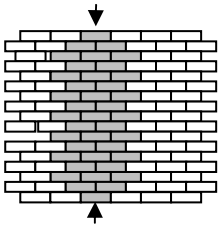

Fig. 7.30. Weak dispersion of a point load

Consequently, evaluating the stresses due to vertical loading calls for working in terms of *vertical* bands

7.3.3.2 Static Schemes of Vertical Wall Bands

Evaluating the stress along vertical wall bands of masonry buildings is a complex problem with various levels of uncertainties particularly dependent on the state of the connections between the walls making up the overall building structure. In old buildings, these connections may be very weak and the walls, particularly of façades, behave much like vertical cantilever beams. In such cases, façade walls can frequently wind up out of plumb. Modern masonry buildings instead apply advanced systems for firmly connecting walls together. At each floor level reinforced concrete ring beams encircle the walls and are connected by slabs to the floor structure. This interconnected system of walls and slab floors produces a stiff 3D cell structure. In some cases, historic buildings, if suitably stiffened, may also present such firmly connected structures. In the event, that an efficient connection system has been fitted to a building, the static behavior of the vertical wall bands can generally be represented by the scheme of a continuous vertical beam with horizontal constraints at the floor level, as illustrated in figure 7.31 *b*). The floor

offsets, produced by the varying wall thickness along the height, activates the floor couples due to the axial load misalignments, as shown in figure 7.32.

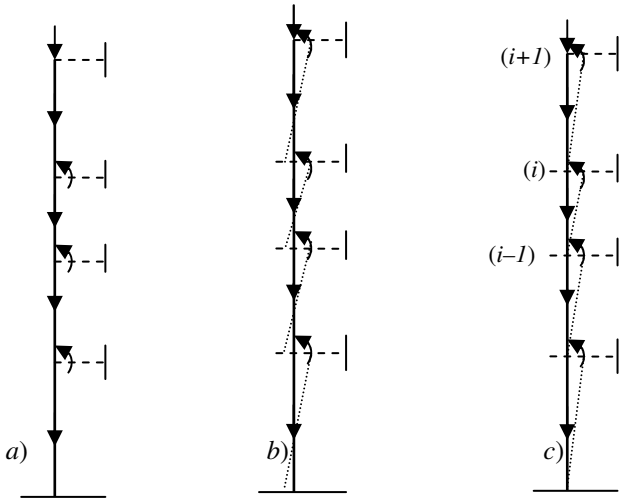

Fig. 7.31. Vertical wall bands with floor couples due to axis misalignments
Bending moment diagrams for actual (*a*) and Building Code schemes (*b*), (*c*)

Figure 7.31 a) shows a vertical beam, representing a wall band of the façade wall, connected at the floor levels to horizontal constraints, which act to oppose bending of the wall band. Due to the different heights of each story and the different thicknesses of the walls between floors, the corresponding continuous beam will have varying spans and sections.

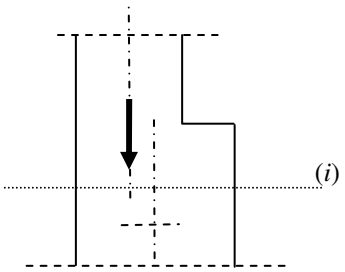

Fig. 7.32. Misalignments between wall axes along the height

Figure 7.31*b* shows a possible diagram of the bending moment along the wall. Note the possible sign inversion in the bending moment diagram at the floor levels. Within this framework, it is useful to cite the simplified approach provided for by the Italian Building Code for evaluating stresses in vertical wall bands. This approach assumes that the wall is hinged at the wall base of each floor, as shown

in Figure 7.31 c). Such an assumption can be justified by considering that, in modern masonry buildings, the presence of the ring beams at each floor interrupts the continuity of the wall, and thereby hinges the wall segments at their base on each floor.

The horizontal forces transmitted to the floors are shown in figure 7.33. At level *i,* the axial load N_i transmitted by the upper wall is *centered.*

Evaluation of the eccentricity at the head of each wall segment, that is, between levels *i* and *i -1*, will consider, together with the centered axial load N_i transmitted by the overlying wall, all other forces transmitted to level *i* by the beam floors in their actual positions, as shown in figure 7.34.

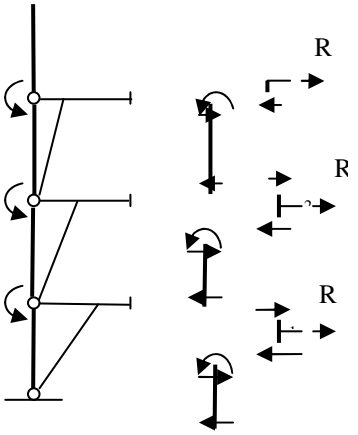

Fig. 7.33. Evaluation of horizontal floor constraints

Thus, the eccentricity *e* of the axial load at the head of the wall segment between levels *i* and *i – 1* can be obtained as

$$e = \frac{N_i d_{i-1} + (\Sigma V_i) d_{vi}}{N_i + \Sigma V_i} \quad . \tag{44}$$

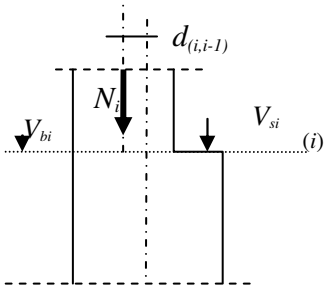

Fig. 7.34. Bending moment evaluation at the head of the wall segment between floors (*i–1*) and (*i*)

The presence of eccentricities in the axial load on the vertical wall bands may induce nonnegligible destabilizing effects that must be adequately accounted for. A simplifying procedure for this purpose is presented in the next section.

7.3.3.3 Simplified Stress Analysis of Wall Bands to Account for the Destabilizing Effects of Axial Loads.

The Italian Building Code (2005) furnishes a useful simplifying approach to account for the destabilizing effects of axial loads on walls and piers. This procedure, which is a modified form of the common ω approach to buckling checks of steel columns, adequately accounts not only for the slenderness ratio λ of the wall, but also for the eccentricity e of the axial load. According to this approach, the mean compression stress in the wall section must be lower than an admissible reference stress $\bar{\sigma}_m$, that is,

$$\sigma = \frac{N}{\Phi A} \leq \bar{\sigma}_m \ , \tag{45}$$

where N is the working axial load acting on the considered wall section, A the geometrical area of the wall section and Φ a suitable strength reduction coefficient that depends on the eccentricity ratio

$$m = 6e/t \tag{46}$$

and the wall slenderness $\lambda = h_o$ /t, where h_o is the inflexion length of the wall, which is in turn given by

$$h_o = \rho h \, , \tag{47}$$

with h the distance between stories, and ρ the side constraint factor. As per Code provisions, this last is taken to be

$$\rho = 3/2 - h/a \quad 0{,}5 \geq h/a \leq 1{,}0 \ ; \ \ \rho = 1/[1+(h/a)^2] \quad 1 > h/a \, , \tag{48}$$

where a indicates the distance between the constraining transverse walls.

Table 6.3 provides the eccentricity ratio factor Φ for various values of wall slenderness and load eccentricity. These values have been obtained through previous analyzes on the destabilizing effects of axial load eccentricities in masonry piers and walls. According to Italian Building Codes, the admissible mean

reference stress $\bar{\sigma}_m$ can be obtained via the characteristic masonry compression strength f_k as

$$\bar{\sigma}_m = f_k / 5 . \tag{49}$$

Table 7.3. Values of eccentricity ratio Φ. They reduce the resistant area of the of the compressed wall section as a function of the wall slenderness and eccentricity factor *m*

h_o/t	*m*=0	*m*=0.5	*m*=1	*m*=1 .5	*m*=2
0	1 .00	0 .74	0 .59	0 .44	0 .33
5	0 .97	0 .71	0 .55	0 .39	0 .27
10	0 .86	0 .61	0 .45	0 .27	0 .15
15	0 .69	0 .48	0 .32	0 .17	
20	0 .53	0 .36	0 .23		

Masonry compression strength, f_k, can also be evaluated by considering the strengths of the individual constituent stones or brick elements and mortar, as discussed in Chapter I.

7.3.3.4 Composite Sections

Composite sections, in which a brick or stone facing covers an inner core of rubble and mortar, are very common in piers and masonry walls. Evaluation of the stresses in such composites must account for the different deformation capacities of the facing and core. Figure 7.35 shows a rectangular composite pier section, for which

$$E_p, \qquad E_n \tag{50}$$

are the elasticity moduli of the different masonries in the pier facing and core, respectively. Let *N* be the axial load acting on the entire section, directed along the pier axis.

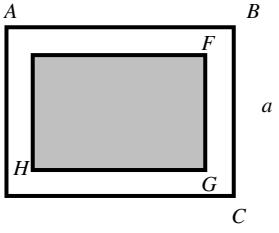

Fig. 7.35. Pier section composed of brick facing and inner rubble core

The mean compressive stresses, σ_p and σ_n, respectively acting on the facing and internal core are unknown. A first relation linking σ_p and σ_n is the following equilibrium equation

$$N = \sigma_p A_p + \sigma_n A_n \ , \tag{51}$$

where A_p and A_n are the areas of the facing and core, respectively. The second relation is the compatibility equation equating the facing and core strains:

$$\varepsilon_p = \varepsilon_n = \varepsilon \ . \tag{52}$$

This condition depends on the bond between the bricks and the core, as well as on the connections potentially existing between the facing and the core. By substituting Eq. (52) into Eq. (53), and accounting for the elasticity relations

$$\sigma_p = E_p \varepsilon_p \qquad \sigma_n = E_n \varepsilon_n \ , \tag{53}$$

we obtain the following expressions for the stresses in the facing and the core:

$$\sigma_p = \frac{N}{A_p + n_{n,p} A_n} \qquad \sigma_n = n_{n,p} \frac{N}{A_p + n_{n,p} A_n} \ , \tag{54}$$

with

$$n_{n,p} = \frac{E_n}{E_p} \ . \tag{55}$$

Note that the destabilizing effects of axial load eccentricities, particularly when dealing with slender piers or walls, are adequately accounted for.

An example
Let us consider the composite section with the following characteristics:
b = 1.50 m; d = 3.00 m; s = 0.30 m;
E_p= 5000 MPa; E_n= 1500 MPa;
N = 500 t.
Thus, we have $n_{n,p} = 0.30$ and

$$\sigma_p = \frac{500}{2.34 + 0.30 \cdot 2.16} 16.73 kg / cm^2 \quad \sigma_n = 5.0 kg / cm^2 \ .$$

7.3.3.5 Mortar Creep Effects

Creep deformations of mortars influence the stress distribution in the facing and core of a composite pier. In evaluating this influence we can assume that creep effects will be greater in the core than in the masonry facing. Thus, considering both creep and shrinkage of the core, recalling the formulation described in Chapter I, the compression stresses in the core and facing

$$\sigma_n(t), \qquad \sigma_p(t) \tag{56}$$

are both functions of time *t*. The compatibility condition is now reformulated as

$$\varepsilon_{ep}(t) = \varepsilon_{en}(t) + \varepsilon_{vn}(t) + \varepsilon_{rs}(t), \tag{57}$$

where $\varepsilon_{en}(t)$, $\varepsilon_{vn}(t)$ e, $\varepsilon_{sn}(t)$ are, respectively the elastic, viscous, and shrinkage strains of the core, and $\varepsilon_{ep}(t)$ the elastic strain of the facing. The elasticity conditions can now be expressed as

$$\sigma_p(t) = E_p \varepsilon_{ep}(t), \qquad \sigma_n(t) = E_n \varepsilon_{en}(t). \tag{58}$$

Considering the creep deformation of the core, Eq. (57) becomes

$$\frac{\sigma_p(t)}{E_p} = \frac{\sigma_n(t)}{E_n} + \frac{\alpha\beta}{E_n} \int_{t_i}^{t} e^{-\beta(\tau - t_o)} \sigma_n(\tau) d\tau + \varepsilon_{sn}(t), \tag{59}$$

where, *t* is the current time and τ any given past time. The equilibrium equation at any time *t* yields

$$N = \sigma_p(t) A_p + \sigma_n(t) A_n \ . \tag{60}$$

Derivation of condition (59) with respect to time *t* gives

$$\frac{d\sigma_p}{dt} = \frac{E_p}{E_n} \frac{d\sigma_n}{dt} + \alpha\beta e^{-\beta(t - t_o)} \sigma_n(t) + E_p \frac{d\varepsilon_{sn}}{dt}, \tag{61}$$

where, recalling Eq. (4) in Section 1.11.4,

$$\frac{d\varepsilon_{rn}}{dt} = \varepsilon_R \beta e^{-\beta(t - t_o)}. \tag{62}$$

The derivative of condition (62) with respect to time t can also be written

$$\frac{d\sigma_p}{dt} = -\frac{A_n}{A_p}\frac{d\sigma_n}{dt} . \tag{62'}$$

Thus, the following equation in the unknown $\sigma_n(t)$ is obtained simply by substituting (62') and (62) into (61):

$$(\frac{A_n}{A_p} + \frac{E_p}{E_n})\frac{d\sigma_n}{dt} + \alpha\beta e^{-\beta(t-t_o)}\sigma_n(t) + E_p\varepsilon_R\beta e^{-\beta(t-t_o)} = 0 . \tag{63}$$

With the position

$$\xi = e^{-\beta(t-t_o)} \tag{64}$$

and accounting for

$$\frac{d\xi}{dt} = -\beta\xi \ , \tag{64'}$$

Eq. (65) becomes

$$-p\frac{d\sigma_n}{d\xi} + \alpha\sigma_n(\xi) \ + \ E_p\varepsilon_{\mathrm{R}} = 0 , \tag{64"}$$

Where

$$p = (\frac{A_n}{A_p} + \frac{E_p}{E_n}) . \tag{65}$$

The solution to (66") is the function

$$\sigma_n(\xi) = Ae^{\frac{\alpha}{p}\xi} - E_p\frac{\varepsilon_R}{\alpha} \ . \tag{66}$$

At the initial time $t = t_i$, that is, at $\xi = \xi_i = e^{-\beta(t_i-t_o)}$, we have

$$\sigma_n(\xi_i) = Ae^{\frac{\alpha}{p}\xi_i} - E_p\frac{\varepsilon_R}{\alpha} = \sigma_{no} \ , \tag{67}$$

where σ_{no} is the purely elastic solution, given by (56). Thus, we obtain

$$\sigma_n(\xi) = (\sigma_{no} + \frac{\varepsilon_R}{\alpha}) e^{\frac{\alpha}{p}(\xi - \xi_i)} - E_p \frac{\varepsilon_R}{\alpha} \ , \tag{68}$$

or more directly

$$\sigma_n(t) = (\sigma_{no} + E \frac{\varepsilon_R}{\alpha}) e^{\frac{\alpha}{p}[e^{-\beta(t-t_o)} - e^{-\beta(t-t_i)}]} - E_p \frac{\varepsilon_R}{\alpha} \ . \tag{69}$$

Similarly, Eq. (60) gives the compression stress in the facing:

$$\sigma_p(t) = \frac{N}{A_p} - \sigma_n(t) \frac{A_n}{A_p} \ . \tag{70}$$

At the limit, for $t \to \infty$, the stresses in the core and facing reach their asymptotic values:

$$\sigma_{n\infty} = (\sigma_{no} + E_p \frac{\varepsilon_R}{\alpha}) e^{-\frac{\alpha}{p} e^{-\beta(t_i - t_o)}} - E_p \frac{\varepsilon_R}{\alpha} \ , \quad \sigma_{p\infty} = \frac{N}{A_p} - \sigma_{n\infty} \frac{A_n}{A_p} \ . \tag{71}$$

If load N is applied to the pier at the same time t_i it takes the mortar to cure, we have $t_i = t_o$ and obtain

$$\sigma_{n\infty} = (\sigma_{no} + E_p \frac{\varepsilon_R}{\alpha}) e^{-\frac{\alpha}{p}} - E_p \frac{\varepsilon_R}{\alpha} , \quad \sigma_{p\infty} = \frac{N}{A_p} - \sigma_{n\infty} \frac{A_n}{A_p} \ . \tag{72}$$

We can now reevaluate the previous example considering the effects of creep and shrinkage of the core mortar. In this case, quantity *p,* defined by (18), is

$$p = (\frac{2{,}16}{2.34} + \frac{5}{1.5}) = 4.256 \ .$$

By assuming $\alpha = 3$, we obtain a/p = 0.705. Considering now that load N = 500 t will act on the pier 1 year after the mortar has cured, we have $e^{-1} = 0.368$, and hence

$$e^{-\frac{\alpha}{p} e^{-\beta(t_i - t_o)}} = e^{-0{,}705 \cdot e^{-1}} = e^{-0{,}705 \cdot 0{,}368} = e^{-0{,}259} = 0.771 .$$

The asymptotic compression stress in the core is thus

$$\sigma_{n\infty} = (\sigma_{no} + E_p \frac{\varepsilon_R}{\alpha}) e^{-\frac{\alpha}{p} e^{-\beta(t_i - t_o)}} - E_p \frac{\varepsilon_R}{\alpha} = (5.02 + 50000X \frac{0.3X10^{-3}}{3}) 0.771 - 50000X \frac{0.3X10^{-3}}{3}$$
$$= 7.725 - 5 = 2.725 \text{ kg/cm}^2.$$

The compression in the facing, on the contrary, is greater than the value resulting from ignoring creep effects:

$$\sigma_{p\infty} = \frac{500}{10 \cdot 2.34} - 2.725 \frac{2,16}{2.34} = 21.37 - 2.51 = 18.85 kg / cm^2 .$$

This result, compared with the elastic solution, reveals the appreciable effect of mortar creep.

7.4 Towers

7.4.1 Introduction

One particular class of masonry buildings, whose height predominates over their widths, are towers in all their forms, including bell towers, minarets, and so forth. *Menhir*, sacred monuments built with gigantic stones, are the most ancient tower-like structures. Of the few livable *menhirs*, the tower in the Wall of Jericho is the most ancient, having been built about 9000 years ago; it is circular in section with a diameter of 8.0 m. Thousands of years later the Sumerians developed constructions called *ziqqurats* – terraced temples with square plans. Only a few traces of these remain today, mainly as the ruins of their foundations. In Italy the *Nuraghi*, built about 3000 years ago, are the most ancient surviving examples of tower constructions.

Towers have often dotted the landscape of many towns, marking their entrance gates, or serving the function of watchtowers or lighthouses. They were also used as symbols of family power, as in San Gimignano, or as church bell towers and mosque minarets. Their height is clearly the characterizing feature of towers, the Lighthouse of Alexandria being one of the highest masonry towers ever built: it was reportedly 120–140 m in height. Built by Greeks in about 305 B.C.E., it collapsed in 1326, though nowadays some traces remain in the Castle of Qaitbay in Egypt.

7.4.2 Typical Cracking Patterns in Masonry Towers

Tower structures have to withstand winds and earthquakes. The action of the wind is probably the most critical because, due to their height, towers have high periods of oscillation and can thereby absorb seismic actions.

In general, high compression stresses must be borne by tower masonry walls, particularly at the lower levels. Such stresses can cause the expulsion of stones and local failures in any irregular masonry. The presence of out-of-plumb walls makes matters worse, because it produces actions orthogonal to the wall plane.

The vertical walls of towers vary considerably in thickness: the tower shaft tends to open and the walls bulge outwards. Thus, vertical cracks frequently occur along the perimeter walls, particularly near window openings and in the upper part of the tower. Figure 7.36 shows a typical cracking pattern in an old, damaged tower, together with a sketch showing the dislodged masonry. The bell tower of St. Mark's Basilica in Venice failed in 1902, as did the Pavia Civic tower in 1989. Both events were probably due to the concurrent effects of all these factors (fig. 7.37).

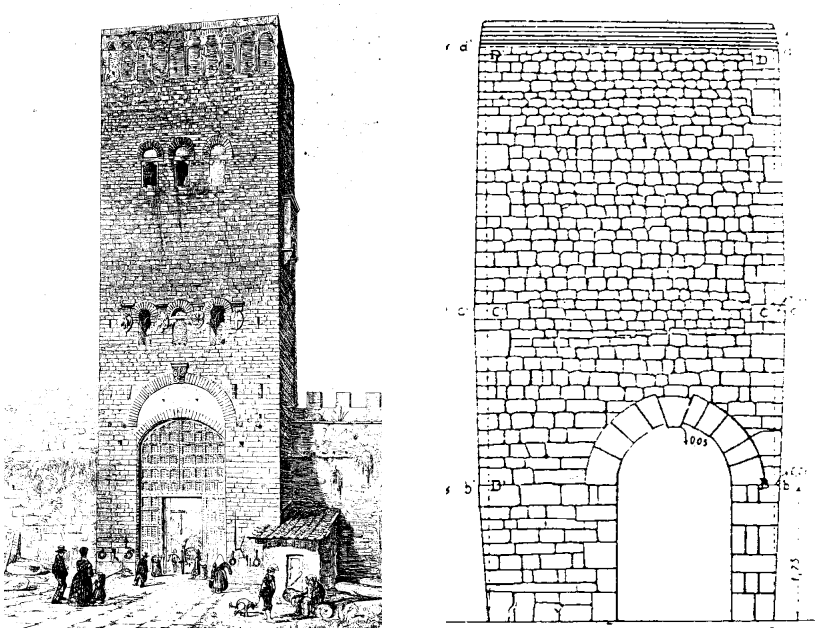

a) b)

Fig. 7.36. *a*) Typical cracking pattern in a masonry tower: the tower of San Niccolò in Florence (from Como, M.T., 2000). B); *b*) dislodged masonry

Surveying cracking patterns can be a difficult task because of towers' heights. Nowadays, thanks to so-called *dynamical structural identification techniques*, tower frequencies and oscillation modes can be measured and different

measurements compared over time, thereby enabling continuous monitoring of the evolution of any damage. One further hazard to towers is lightening. Humidity can collect in cracks, which makes the structure a good conductor of electricity. Thus, if the tower is struck by lightening, the instantaneous increase in temperature of the humid air present in the cracks gives rise to an actual explosion within the masonry. This explains why old steeples and towers are frequently heavily damaged by lightening bolts. A clear lesson to be learned from this is that tower masonry must always be maintained in good condition.

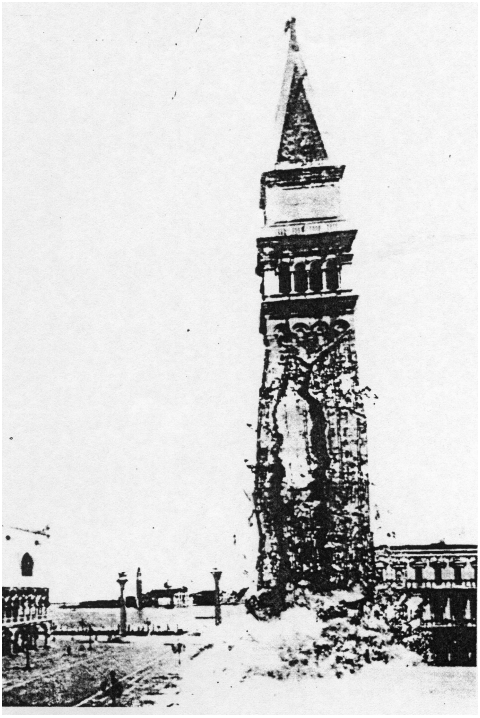

Fig. 7.37. Failure of the Bell Tower of St. Mark's in Venice in 1902, from a photo by L.H.N. Dufour, (De Fez, 1982)

In bell towers, the vibrations setup by the bells themselves may be a source of damage, hence checks of the vibrations induced by the motion of bells is frequently performed on such structures. Typical restoration works include masonry refurbishment and ringing with steel ties at various levels to restore the connections between the walls.

Serious static problems frequently depend on towers' foundations, which produce stress on narrower soil areas in comparison to ordinary buildings.

Differential settling frequently occurs with consequent appreciable inclination and rotation of the tower. So-called *leaning stability* analysis is a problem particular to the statics of towers resting on deformable soils (Hambly, 1985, Como, 1993). The research on determining a suitable foundation model for towers is addressed in the following sections.

7.4.3 Plastic Foundation Model

There are a number of different models for foundations that seek to describe their static response. These include both linear and nonlinear elastic approaches (see for instance, Hambly, 1985), though plastic or visco-plastic models may be more appropriate. A tower involves the presence of high stresses in the foundation. Tilting of the tower, occurred during its construction, thereby confirming the strong stresses at their bases, moreover suggests that the underlying soil is at the plastic state.

Simple plastic and visco-plastic foundation models, following the basic approach of Meyerhof (1951), will thus be covered in detail in the next sections. Now let us consider a foundation plinth resting on the soil (fig. 7.38) under the action of a centered axial load N and moment M, such that their resultant remains applied internally to the plinth. By gradually assigning increments to N and M, at a given point in the loading path, the plinth undergoes significant subsidence due to the plastic deformations occurred in the underlying soil.

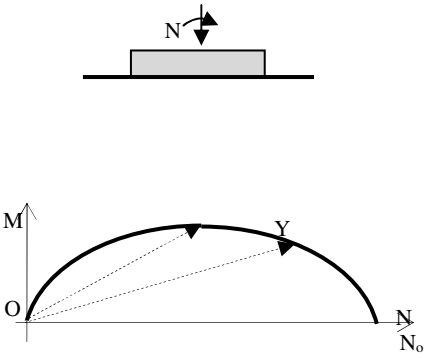

Fig. 7.38. Yield locus of a foundation eccentrically loaded and supported by noncohesive soil

By assuming different ratios between M and N (i.e., different eccentricities of N with respect to the center of the base section of the plinth), we can apply different loading paths and trace the locus Y of the points (M, N) in the plane M, N defining the attainment of the plastic state, also called the limit state. A typical interaction locus Y between the vertical load N and moment M, is drawn in figure 7.38, which

outlines the various soil limit states. For the sake of simplicity, let us assume that the foundation is rectangular with width a and transverse length b, and, according to Meyerhof (1951), let us also assume that *in the plastic state* a constant pressure p_o pushes on the compressed soil. In particular, if the foundation is centrally loaded, the limit load $N_o = p_o ab$ represents the ultimate centered vertical load, that is to say, the ultimate bearing capacity of the foundation under a centered vertical load. We can moreover assume (fig. 7.39) that the supporting soil section of the plinth, eccentrically loaded, is subjected to a constant distribution of limit pressure p_o and engages only a band of limited width, equal to $(a/2 - x)$. Thus, the plinth equilibrium in the vertical direction yields

$$(\frac{a}{2} - x) = \frac{Na}{N_o} \ . \tag{73}$$

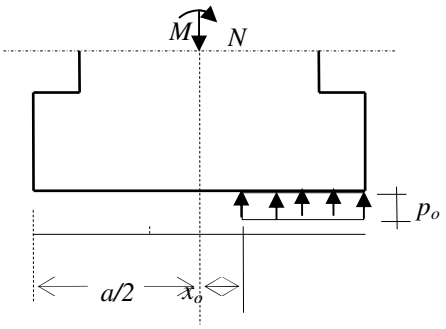

Fig. 7.39. Plastic model of an eccentrically loaded foundation

At the same time, rotational equilibrium yields

$$M = \frac{Na}{2}(1 - \frac{N}{N_o}) \ . \tag{74}$$

Equation (74) describes the plastic state in terms of N and M and indicates the interaction locus in the plane $M,N,$ as sketched out in figure 7.38. Generally, the interaction locus is represented by an equation of the type

$$f(M, N, N_o) = 0 \ . \tag{75}$$

Thus, for a rectangular foundation, taking (74) into account, we have

$$\text{s}\, f(M, N) = M - \frac{Na}{2}(1 - \frac{N}{N_o}) = 0 \ . \tag{76}$$

The stress vector representing the loads acting on the foundation can be expressed by a two-component vector

$$\sigma = \begin{bmatrix} M \\ N \end{bmatrix}, \tag{77}$$

disregarding the negligible shear. We can now evaluate the response of the foundation to an increase in stress. The corresponding plastic deformation increment is given by the two-component vector

$$d\varepsilon = \begin{bmatrix} d\theta \\ dv \end{bmatrix}, \tag{78}$$

where $d\theta$ is the plastic rotation and dv the increase in the plastic settlement. When the loading path reaches a point P on locus Y, a plastic strain increment $d\varepsilon$ of the plinth occurs and has both components $d\theta$ and dv. These plastic strain increments develop both when the loading point P remains fixed on the locus as well as when P moves along it. To define the strain increment, we can thus move the loading point P along Y by applying a small increment $d\boldsymbol{\sigma}$ *tangent* to Y. The plastic strain increment $d\boldsymbol{\varepsilon}$ will occur without any work by $d\boldsymbol{\sigma}$, in compliance with the basic principles of the Theory of Plasticity (fig. 7.40).

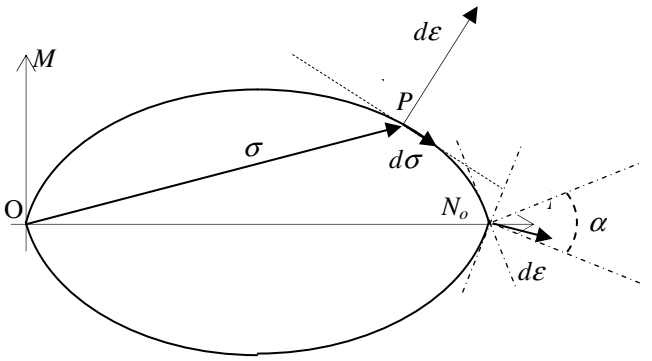

Fig. 7.40. Normality rule for a plastic strain increment

If we move along the yield locus, the plastic deformation occurs without energy expense, hence

$$d\sigma \cdot d\varepsilon = 0 \ . \tag{79}$$

Condition (79) indicates the orthogonality of $d\varepsilon$ to the boundary of locus Y (fig. 7.40). The plastic strain increment $d\boldsymbol{\varepsilon}$ is thus given by

$$d\varepsilon = \lambda \frac{\partial f}{\partial \sigma} \quad \lambda>0 \quad \text{se } df > 0, \quad \lambda = 0 \quad \text{se} \quad df \le 0 \quad , \tag{80}$$

where $f(\sigma)$ is given by Eq. (80) and df is its differential.

At the centered axial loading point ($N = N_o$, $M = 0$) the interaction locus presents a vertex, and the corresponding strain rate $d\varepsilon$ is a vector having any direction within the angle α and will include both plastic settlement and rotation, as shown in figure 7.53. This result explains the possible occurrence of a *sudden tilting* of the tower during its construction, when its weight, centrally applied on the foundation, reaches the limit value N_o. In particular, from (80), for a rectangular foundation we have

$$\frac{\partial f}{\partial M} = 1 \qquad \frac{\partial f}{\partial N} = a\left(\frac{N}{N_o} - \frac{1}{2}\right) \tag{81}$$

and

$$d\theta = \lambda \qquad dv = (-x)\lambda = -x\, d\theta \ . \tag{82}$$

According to (82), the plastic strain increment is thus produced by a rotation $d\theta$ of the foundation base section around the neutral axis corresponding to the current loading condition. This property holds for any type of foundation (fig. 7.41).

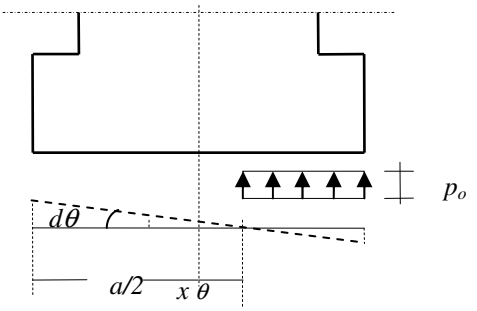

Fig. 7.41. Kinematic consequence of the plastic behavior of an eccentrically loaded foundation

7.4.3.1 Subsequent Yield Loci of Plastic Hardening Soils

Loose or weakly consolidated soils actually become stronger as loading progresses. The behavior of the foundation soil of tilting towers can often be explained by the presence of such soils. Soil strain hardening occurs as the soil deformations increase and a sequence of subsequent yield loci develops, as shown in figure 7.55. The first plastic state is represented by the first locus Y_{oo}, while the

final collapse state of the soil corresponds to the final locus Y_R. The plastic strain rate can thus be expressed via the following associated flow rule;

$$d\varepsilon = \frac{1}{\chi}\frac{\partial f}{\partial \sigma}\mathrm{d}f \quad \text{if } df > 0 \text{ and} \quad \mathrm{d}\varepsilon = 0 \quad \text{if} \quad \mathrm{d}f \le 0 \quad , \tag{83}$$

where $\chi(\sigma)$ indicates the *strain hardening function* of the soil. This function will be determined for a tower foundation in the next section.

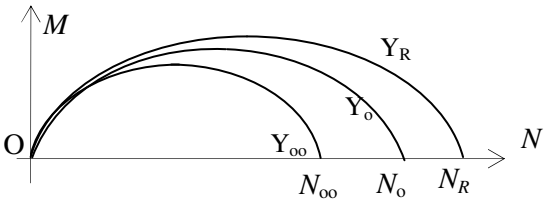

Fig. 7.42. Subsequent yield loci for a strain hardening foundation

7.4.3.2 The Moment–Plastic Rotation Equation for a Tower Foundation

With reference to the case of a tower foundation, it should be noted that increasing the tower's tilt (fig. 7.43) causes an increase in moment *M,* while the axial load *N* remains practically constant. A shear force acting on the foundation also occurs, though it is so small as to be negligible.

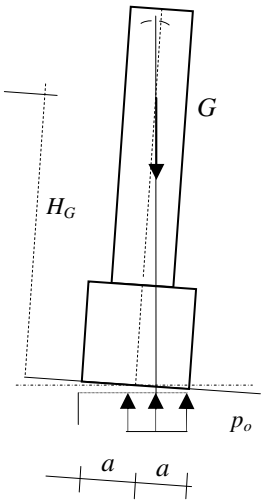

Fig. 7.43. A tilting tower

The strain hardening function $\chi(\sigma)$ can be considered to depend solely on the moment M via the function

$$\chi(M) \tag{84}$$

This function represents softening behavior, that is, a gradual reduction in its tangent modulus as the rotation increases. It will also be able to describe *failure* of the foundation under the ultimate value of moment M_R, that is, the occurrence of unbounded values of plastic rotations under the failure moment M_R. To construct this function, note that with N = cost, we have

$$df = dM \quad , \tag{85}$$

and the corresponding rotation increment, with the assumption of a rectangular base foundation, is

In particular, for a rectangular plinth

$$d\theta = \frac{1}{\chi(M)} dM \ , \tag{86}$$

and the strain hardening function is given by

$$\chi(M) = \frac{dM}{d\theta} . \tag{87}$$

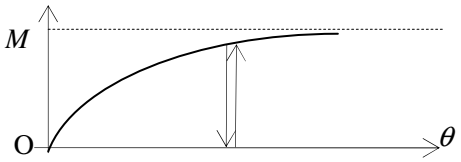

Fig. 7.44. Moment–rotation diagram

This strain hardening function, $\chi(M)$, defines the rotational tangent modulus and can be expressed as

$$\chi(M) = K_{\theta o} \frac{M_R - M}{M_R}, \tag{88}$$

where $K_{\theta o}$ is the initial tangent modulus, that is, the derivative $dM/d\theta$ at $M = 0$. With this position we thus get

$$d\theta = \gamma_{oR} \frac{dM}{M_R - M} \quad , \tag{89}$$

where

$$\gamma_{oR} = \frac{M_R}{K_{\theta o}} \quad . \tag{90}$$

The quantity γ_{oR} can be defined as the *foundation deformability factor*. From (89) it can be seen that when the acting moment approaches the failure moment M_R, the rotation increment rises without limit. Integration of Eq. (89) gives (Como, 1993)

$$M(\theta) = M_R (1 - e^{-\frac{\theta}{\gamma_{oR}}}) \quad . \tag{91}$$

Equation (91) describes the moment – rotation law of a rigid foundation resting on strain hardening soil. Upon unloading, permanent rotations occur, as shown in figure 7.44.

7.4.4 Stability of Leaning Towers

We assume that sudden, nonuniform soil settlement has taken place, with a consequent initial rotation θ_{oi} of the tower.

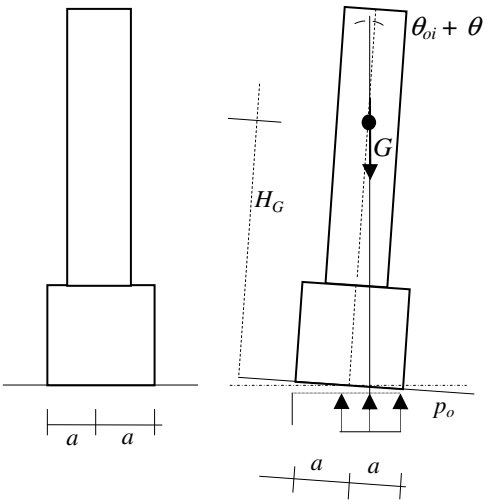

Fig. 7.45. Equilibrium of a leaning tower consequent to an initial rotation θ_{oi} of the foundation

The tower will consequently undergo an additional instantaneous rotation θ due to the supervening eccentric position of weight G. The foundation base is thus loaded by the stress components (fig. 7.45):

$$N = G\cos(\theta_{oi} + \theta) \qquad M = GH_G \sin(\theta_{oi} + \theta) \qquad T = G\sin(\theta_{oi} + \theta) \tag{92}$$

We also assume that in the past the tower has never undergone tilting rotations larger than the current one. During the loading history, the actual yield locus Y will thus never be contained within larger loci. The loading point $P(M, N)$, with components N and M given by (94), is thus located over the yield function Y (fig. 7.46). Rotational equilibrium of the tower gives

$$GH_G \sin(\theta_{oi} + \theta) - M_R(G)\left(1 - e^{-\frac{\theta}{\gamma_{oR}(G)}}\right) = 0 \ . \tag{93}$$

Equation (93) equalizes the overturning moment given by the second of (92) to the resisting moment (91). Equation (93) can be symbolically expressed as

$$g[G(\theta), \theta] = 0 \tag{94}$$

and shows the dependence of weight G on the rotation θ.

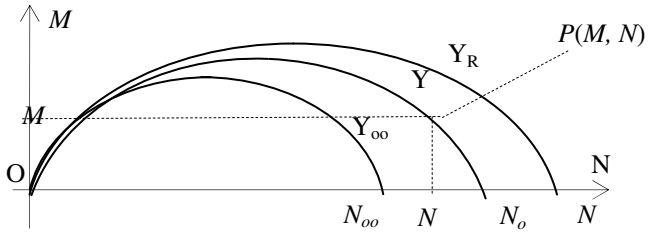

Fig. 7.46. Loading state of a tilted tower foundation

By differentiating this condition, we get

$$\frac{\partial g}{\partial G}\frac{dG}{d\theta} + \frac{\partial g}{\partial \theta} = 0 \tag{95}$$

and then obtain

$$\frac{dG}{d\theta} = -\frac{\partial g}{\partial \theta} \Big/ \frac{\partial g}{\partial G} \ . \tag{96}$$

The denominator term in (98) does not vanish. The equilibrium of the tower becomes critical if

$$dG / d\theta = 0 \quad . \tag{97}$$

In the critical state, increments in the tower's rotation occur, in fact, without any further increments in the weight G. Specifically, Eq. (97) gives

$$\frac{dG}{d\theta} = \frac{\partial g}{\partial \theta} = GH_G \cos(\theta_{oi} + \theta) - K_{\theta o} e^{-\theta/\gamma_{oR}} = 0 \quad . \tag{98}$$

The rotational equilibrium is preserved in the critical state as well. Condition (98) will thus be associated with rotational equilibrium condition (93). From these equations, the two unknowns – the critical weight G^*_{cr} and the critical rotation θ^* of the tower – can be determined. Eqs. (93) and (98) yield the following condition

$$tg(\theta_{oi} + \theta^*) = \gamma_{oR}(e^{\theta^*/\gamma_{oR}} - 1) \quad , \tag{99}$$

which, for small values of $(\theta_{oi} + \theta^*)$, gives

$$\theta^* \approx \sqrt{2\gamma_{oR}\theta_{oi}} \quad . \tag{100}$$

The critical weight of the tower $G^*_{cr}(\theta_{oi})$ can be obtained from Eqs. (100) and (98). We thus have

$$\frac{G^*_{cr} H_G}{K_{\theta o}} = \frac{e^{-\theta^*/\gamma_{oR}}}{\cos(\theta_{oi} + \theta^*)} \quad . \tag{101}$$

As θ_{oi} becomes smaller and smaller, θ^* also vanishes and the critical weight becomes

$$\lim_{\theta_{oi} \to 0} G^*_{cr} = G_{cro} \quad , \tag{102}$$

where

$$G_{cro} = \frac{K_{\theta o}}{H_G} \quad . \tag{103}$$

The critical weight G_{cro} represents the critical weight of the *initially vertical* tower. Substitution of (103) into (101) gives the explicit expression for the critical weight of a leaning tower (Como M., 1993):

$$\frac{G_{cr}^{*}}{G_{cro}} = \frac{e^{-\theta^{*}/\gamma_{oR}}}{\cos(\theta_{oi} + \theta^{*})} \quad . \tag{104}$$

The critical tower weight has also been evaluated by Nova and Montrasio (1995).

Equation (104) shows that even a small initial rotation θ_{oi} of the tower can produce a large reduction in the critical weight G_{cr}^{*} with respect to the value G_{cro} of the critical weight of a vertical tower (fig. 7.47). Such a critical condition is unstable.

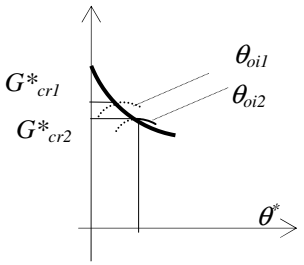

Fig. 7.47. Variation of the tower critical weight G_{cr}^{*} with initial rotation θ_{oi}

We can define a factor, *s,* that expresses the safety of a tower in its rotated configuration. This safety factor is given by

$$s = \frac{G_{cr}^{*}}{G} \quad , \tag{105}$$

where G_{cr}^{*} is the critical weight of the tower that has undergone an initial subsidence rotation θ_{oi}. As long as coefficient *s* is not too small, the leaning tower will remain in its tilted position in a stable state, as has occurred, for instance, for the Garisenda tower in Bologna. To the contrary, if *s* is near unity, the tower equilibrium is quite uncertain. In such cases, small changes in the loads or in environmental conditions can lead to failure of the tower. Furthermore, creep deformations of the soil may lead to slowly increasing tilting of the tower.

Various systems can be used to improve the safety of towers. Some aim to reduce their inclination. The following sections will address these issues, with a particular focus on stability analysis of the renowned Leaning Tower of Pisa and the work carried out to stabilize it.

7.4.5 Counter Weights to Stabilize Leaning

Given the attempts made to stabilize a number of leaning towers in this fashion, it is interesting to evaluate the response of such structures to the application of counter weights. To this end, let us consider the scheme in figure 7.48, where an additional weight ΔP has been placed on the base of a leaning tower on the side opposite its inclination.

The plastic response of the foundation is different from the elastic case. According to the elastic foundation model, application of load ΔP on the side opposite the tilt would certainly reduce the tower's inclination. The stress acting on the foundation, before application of the additional load ΔP, is localized at point A of the interaction domain Y, corresponding to an assigned level of hardening N_o. The coordinates of this point, A, in the plane M, N are

$$N \approx G \qquad M = GH_G \sin(\theta_{oi} + \theta) \tag{106}$$

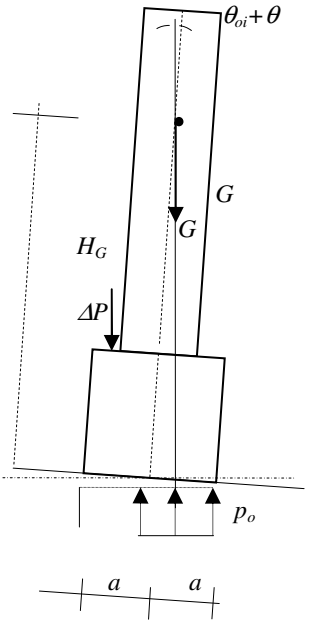

Fig. 7.48. Application of a counter weight on a leaning tower

According to the elastic model, the foundation response is represented by an increase in subsidence, together with a negative increment, $d\theta$, that is, counter rotation of the tower. According to the plastic model, instead, the foundation strain

rate will, be the normality rule, directed along the external normal at A to the interaction locus Y. Consequently, if $df > 0$, the rotation rate $d\theta$ will be positive and a further increase in the tower's inclination will occur (fig. 7.49). The differential df of the yielding function f at A is, on the other hand, given by

$$df = (\frac{\partial f}{\partial M})_A dM + (\frac{\partial f}{\partial N})_A dN , \tag{107}$$

which, in the simple case of rectangular foundations, by accounting for (81), yields

$$df = -\Delta N e + \Delta N(-\frac{1}{2} + \frac{N}{N_o}) = (-e - \frac{a}{2} + \frac{Na}{N_o})\Delta N . \tag{108}$$

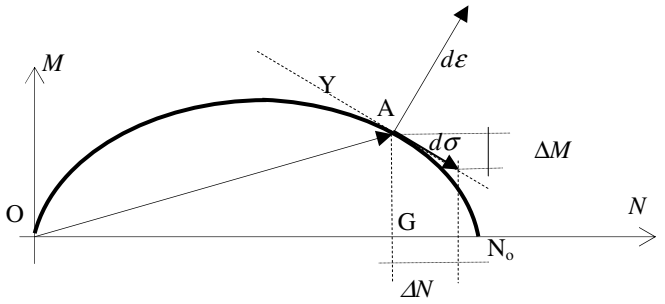

Fig. 7.49. Response $d\varepsilon$ of a plastic foundation to stress increment $d\sigma$

Let

$$e_L \tag{109}$$

be the *limit* eccentricity value, which corresponds to a zero increment in plastic rotation of the foundation, that is, when $df = 0$. Hence, we get

$$e_L = a(\frac{N}{N_o} - \frac{1}{2}) . \tag{110}$$

Moreover, accounting for (110) and that

$$2H_G(\theta_{oi} + \theta) = x + \frac{a}{2} , \tag{111}$$

the limit eccentricity becomes

$$e_L = a[\frac{1}{2} - \frac{2H_G}{a}(\theta_{oi} + \theta)] \ . \tag{110'}$$

Consequently, we can write

$$df = (e_L - e)\Delta N \ , \tag{110"}$$

and we can thus conclude that only when

$$e > e_L \tag{112}$$

will $df < 0$ (fig. 7.49). For instance, in the case of a rectangular foundation of width a, with $2H_g/a = 2.5$, $(\theta_{oi} + \theta) = 5°$, it can be seen that an eccentricity value $e = a/4$ is insufficient to ensure $e > e_L$.

7.4.6 An Attempt to Analyze the Evolution in Time of Tower Tiling

7.4.6.1 Soil Creep Effects on Leaning Tower Equilibrium

Leaning towers frequently attain a tilting configuration that remains unchanging over time. In such cases, the foregoing analysis can be deemed suitable for checking their stability. In other cases, however, such as for instance, the leaning Tower of Pisa, a structure may undergo slow but progressive increases in tilting. The equilibrium state of the tower evolves over time and can either stabilize asymptotically or deteriorate until it reaches failure.

The evolution of a tower's rotation depends on the behavior of the foundation soil, whose response changes over time. There are various reasons for this behavior: periodic variations in the height of the water table linked to particular soil features, as creep of the solid particles of the soil itself, amongst others. Moreover, the interactions occurring between the time-dependent foundation soil response and the tower's tilting are extremely important. A small, uneven settling of the foundation causes an increase in rotation that, in turn, leads to greater axial load eccentricity on the foundation and consequently slow further tilting of the structure, and so on. A simple visco-plastic foundation model can describe this behavior. To this end, accurate geotechnical techniques are available to define the visco-plastic soil parameters involved in the various cases.

7.4.6.2 Visco-Plastic Model of Foundations

A visco-plastic model of the foundation can explain variations in a tower's inclination over time. A simple visco-plastic model considers the strain rate $\dot{\varepsilon}$ expressed as the sum of the plastic and viscous shares

$$\dot{\varepsilon} = \dot{\varepsilon}^p + \dot{\varepsilon}^v \ , \tag{113}$$

where the plastic strain rate $\dot{\varepsilon}^p$ is given by (80) and the viscous rate $\dot{\varepsilon}^v$, according to a common rheological equation, is given by

$$\sigma = K_v \dot{\varepsilon}^v \tag{114}$$

The stress vector, σ, of components M and N is given by (77), where K_v is the foundation viscous stiffness matrix:

$$K_v = \frac{1}{\alpha} e^{\beta(t-t_o)} \begin{bmatrix} k_{\theta\theta} & 0 \\ 0 & k_{vv} \end{bmatrix}. \tag{115}$$

In expression (115), t_o indicates the initial time, corresponding to completion of the tower, when it is assumed that the load began to act. The constant α is a factor expressing the intensity of the viscous deformation of the foundation, β a scale factor assumed equal to 1 century^{-1}, and $k_{\theta\theta}$, k_{vv} are positive quantities defining the viscous behavior of the foundation. The assumed viscous constitutive equation conforms to the formulation of creep deformation discussed in Chapter I. Equation (114) can be written in the more explicit form:

$$\begin{bmatrix} M(t) \\ N(t) \end{bmatrix} = \frac{1}{\alpha} e^{\beta(t-t_o)} \begin{bmatrix} k_{\theta\theta} & 0 \\ 0 & k_{vv} \end{bmatrix} \begin{bmatrix} \dot{\theta}_v \\ \dot{v}_v \end{bmatrix}. \tag{115'}$$

Hence, we get

$$M(t) = \frac{1}{\alpha} e^{\beta(t-t_o)} k_{\theta\theta} \dot{\theta}_v \qquad N(t) = \frac{1}{\alpha} e^{\beta(t-t_o)} k_{vv} \dot{v}_v \tag{116}$$

or

$$\dot{\theta}^v = \frac{\alpha}{k_{\theta\theta}} e^{-\beta(t-t_o)} M(t) \qquad \dot{v}^v = \frac{\alpha}{k_{vv}} e^{-\beta(t-t_o)} N(t) \tag{116'}$$

.

For a better understanding of the mechanical significance of the various parameters involved according to the proposed visco-plastic model, as a first step let us analyze the slow subsidence of a foundation under *constant* loads, *G* or *M,* resting on a purely viscous soil, whose behavior is defined by Eq. (115'). Thus, from Eq. (115'), we get

$$\dot{\theta}^v = \frac{\alpha}{k_{\theta\theta}} e^{-\beta(t-t_o)} M \qquad \dot{v}^v = \frac{\alpha}{k_{vv}} e^{-\beta(t-t_o)} N \tag{116"}$$

.

Integration of (116") gives (fig. 7.50)

$$\theta^v(t) = \frac{\alpha}{\beta k_{\theta\theta}} M[1 - e^{-\beta(t-t_o)}] \qquad v^v(t) = \frac{\alpha}{\beta k_{vv}} G[1 - e^{-\beta(t-t_o)}] \tag{117}$$

The asymptotic values of the foundation rotation and settlement are thus

$$\theta^v_\infty = \frac{\alpha}{\beta k_{\theta\theta}} M \qquad v^v_\infty = \frac{\alpha}{\beta k_{vv}} G \tag{118}$$

The quantities

$$\frac{\beta k_{\theta\theta}}{\alpha} \qquad \frac{\beta k_{vv}}{\alpha} \tag{119}$$

represent the rotational and vertical asymptotic viscous stiffness of the foundation.

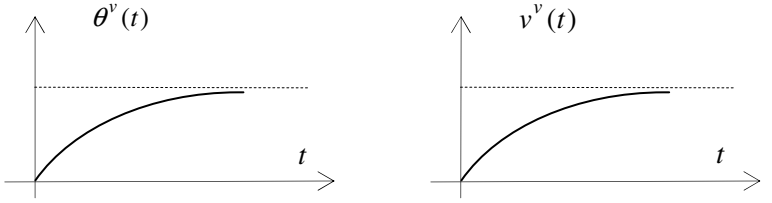

Fig. 7.50. Evolution laws of the subsidence and rotation of a purely viscous foundation under constant centered vertical load and constant couple

7.4.6.3 Slow Tilting of Towers Resting on Visco-Plastic Foundation

Let us now consider a tower on visco-plastic soil, defined by the model discussed above. The tower undergoes an initial tilt θ_{oi} due to differential subsidence of the foundation at the onset of its construction. The initial equilibrium configuration of the tower is thus rotated: this initial inclination causes load G to become eccentric and slowly, over time, produces visco-plastic strains and further tilting. The slow displacement of the tower will be characterized by a predominating rotational component $\theta(t)$, which occurs under nearly constant axial load. Here, $\theta(t)$ now represents the *entire* rotation of the tower at time t, including the initial tilt as well as the visco-plastic share.

In light of previous results, we can disregard the contribution to the displacement of the small changes in the axial load during progressive tilting.

The rotation rate at time t is due to the strong interactions between the two plastic and viscous portions:

$$\dot{\theta}(t) = \dot{\theta}^{p}(t) + \dot{\theta}^{v}(t) \ . \tag{120}$$

Creep rotation in fact produces rotation increments and, consequently, increases in the moment $M(t)$ acting on the foundation. This monotonically increasing moment, in turn, produces further increments in the plastic rotation and so on. The hardening of the soil, which slowly reduces the magnitude of the viscous rotation rates, conflicts with the increasing moment $M(t)$, whence new, additional rotation arises. Once this process has been initiated, either the tower's movement will slowly stabilize or it will progress fatally toward failure. In this context, from Eq.(120), and by accounting for (89) and the first Eq. (117) , we get

$$\dot{\theta} = \frac{M_R}{K_{\theta o}} \frac{\dot{M}}{M_R - M(t)} + \frac{M(t)}{k^{v}_{\theta\theta}} \alpha e^{-\beta(t-t_o)} \ . \tag{121}$$

The moment $M(t)$ acting on the foundation is given by

$$M(t) = GH_G \sin\theta(t) \ . \tag{122}$$

Thus, taking into account that

$$\dot{M}(t) = GH_G \dot{\theta} \cos\theta(t) \, , \tag{123}$$

from Eq. (121), we have

$$\dot{\theta} = \frac{M_R}{K_{\theta o}} \frac{\dot{\theta}\cos\theta(t)}{\mu_R - \sin\theta(t)} + \frac{\alpha}{k^{v}_{\theta\theta}} e^{-\beta(t-t_o)} GH_G \sin\theta(t) \, , \tag{124}$$

where

$$\mu_R = \frac{M_R}{GH_G} \ . \tag{125}$$

With the position

$$\phi(t) = \mu_R - \sin\theta(t) \tag{126}$$

and taking into account that

$$\dot{\phi} = -\dot{\theta}\cos\theta(t) \ , \tag{126'}$$

Eq. (124) gives

$$-\frac{M_R}{K_{\theta o}}\frac{\dot{\phi}}{\phi} + \frac{\mu_R \alpha}{\overset{v}{\chi}_{\theta\theta}} e^{-\beta(t-t_o)} - \frac{\alpha\phi}{\overset{v}{\chi}_{\theta\theta}} e^{-\beta(t-t_o)} = -\frac{\dot{\phi}}{\cos\theta} \ , \tag{127}$$

The factor (128) where

$$\overset{v}{\chi}_{\theta\theta} = \frac{\overset{v}{k}_{\theta\theta}}{GH_G} \tag{128}$$

represents the dimensionless rotational viscous stiffness of the foundation. With the change in variable

$$\xi = e^{-\beta(t-t_o)} \ , \tag{129}$$

and accounting for

$$\phi = \phi[\xi(t)] \qquad \dot{\phi} = -\phi'\beta\xi \qquad (\ )' = \frac{d(\ )}{d\xi} , \tag{130}$$

we get

$$\frac{M_R}{K_{\theta o}}\beta\frac{\phi'}{\phi} + \frac{\mu_R \alpha}{\overset{v}{\chi}_{\theta\theta}} - \frac{\alpha}{\overset{v}{\chi}_{\theta\theta}} = \beta\frac{\phi'}{\cos\theta} \quad . \tag{131}$$

Thus, by taking position (126) into account, after some manipulations we obtain

$$\frac{\beta\overset{v}{\chi}_{\theta\theta}}{\alpha}\frac{(\dfrac{1}{\cos\theta} - \dfrac{\gamma_{oR}}{\mu_R - \sin\theta})}{\sin\theta}(-\cos\theta d\theta) = d\xi \tag{132}$$

Separation of variables gives

$$\xi = -\frac{\beta\overset{v}{\chi}_{\theta\theta}}{\alpha}\int\frac{1 - \dfrac{\gamma_{oR}\cos\theta}{\mu_R - \sin\theta}}{\sin\theta}d\theta + k \tag{133}$$

and by integrating we get

$$\xi = 1 + \frac{\beta \chi^{v}_{\theta\theta}}{\alpha} [\ln(tg \frac{\theta}{2}) - \frac{\gamma_{oR}}{\mu_R} \ln(\frac{\sin\theta}{\mu_R - \sin\theta})] + k \quad . \tag{134}$$

Let us assume, for the sake of simplicity, that

$$t_o = 0 \ .. \tag{135}$$

Then $\xi(t_o = 0) = 1$, and the initial conditions are

$$\theta = \theta_i \ \text{ at } \xi = 1 . \tag{136}$$

Thus, we obtain the explicit formulation of function $\xi = \xi(\theta)$:

$$\xi = 1 + \frac{\beta \chi^{v}_{\theta\theta}}{\alpha} \{\ln[\frac{tg(\theta_i / 2)}{tg(\theta / 2)}) - \frac{\gamma_{oR}}{\mu_R} \ln(\frac{\mu_R - \sin\theta_i}{\mu_R - \sin\theta} \frac{\sin\theta}{\sin\theta_i})] \tag{137}$$

that describes the evolution of the leaning of the tower over time.

7.4.6.4 Critical State. Critical Time

Different, but *simultaneous,* equilibrium configurations occur at the critical state.

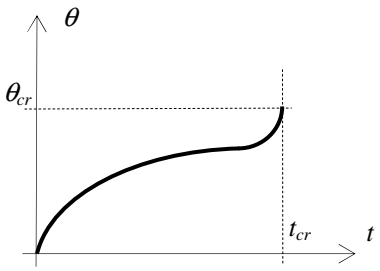

Fig. 7.51. The critical state

Thus, in the critical state

$$\frac{dt}{\mathrm{d}\theta} = 0 \quad , \tag{138}$$

or, taking (129) into account,

$$\frac{d\xi}{d\theta} = 0 \quad . \tag{138'}$$

However, from (138) and (137), the critical condition becomes

$$\frac{1}{\cos\theta} - \frac{\gamma_{oR}}{\mu_R - \sin\theta} = 0 \quad , \tag{139}$$

which gives the equation for the critical rotation

$$\gamma_{oR}\cos\theta_{cr} + \sin\theta_{cr} = \mu_R \quad , \tag{140}$$

which, in turn, furnishes θ_{cr} with the assigned values of μ_R and γ_{oR}. Substituting this value of θ_{cr} into Eq. (137) yields the critical time. The condition,

$$\xi_{ct} \in [0,1] \quad , \tag{141}$$

indicates whether or not the critical state can be actually be attained. Figure 7.51 shows the plot $\theta(t)$ of the tower rotation versus time. At the critical state, defined by the coordinates, critical time t_{crit}, and critical rotation θ_{crit}, the tangent to the curve $\theta(t)$, according to (138), becomes vertical. The impending critical state is signaled by the change in sign of the derivative $d\theta / dt$, from negative to positive values, implying *acceleration* of the motion.

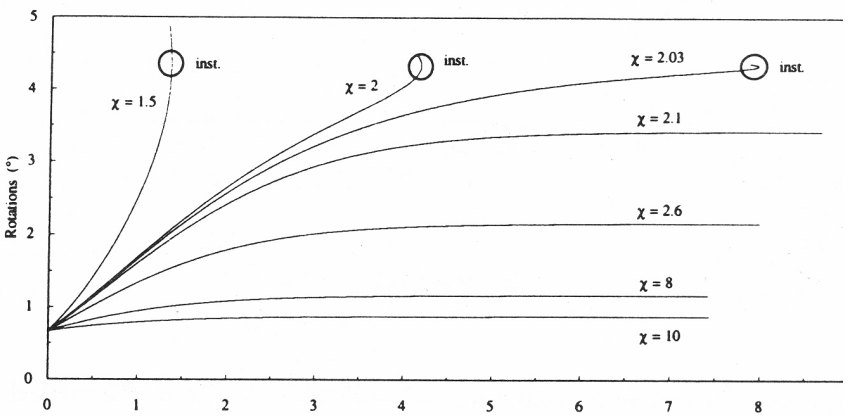

Fig. 7.52. Plot of the rotation versus time (in centuries) of a leaning tower with an initial tilt, resting on a visco-plastic foundation for different values of the dimensionless asymptotic viscous stiffness

We have applied the proposed visco-plastic model to analyzing the slow rotation of a leaning tower by assuming the values of M_R and of $K_{\theta 0}$ considered in the

next section. Figure 7.52 shows the plot of the tower inclination versus time, expressed in centuries, for various values of the dimensionless foundation asymptotic viscosity stiffness. All possible behaviors of such a tower can be described by varying the different quantities involved. Small values of the dimensionless foundation viscous stiffness, which also signify high, heavy towers, led to leaning failure.

7.4.7 The Leaning Tower of Pisa

The Tower of Pisa (fig. 7.53) was designed as a cylindrical belfry that would stand about 56 m high. The width of its walls varies from 4.09 m at its base to 2.48 m at the top. The Tower is a hollow cylindrical shaft with eight stories, including the bell chamber. The external and internal diameters at the base are about 15.5 and 7.4 m, respectively. The bottom story is made up of 15 marble arcades, while each of the next six stories contains 30 arcades surrounding the inner cylinder of the tower. The top story is the bell chamber itself, with 16 arcades. The inner and outer surfaces are faced with marble and the annulus between these facings is filled with rubble and mortar within which extensive voids have been found.

Construction of the Tower, the Cathedral's bell tower, had a troubled history. Construction was begun in 1173, probably under the supervision of Bonanno Pisano. However, the Tower already began to sink after construction had progressed to the second floor in 1178. This was due to a mere 3 m-deep foundation, set in weak, deformable subsoil. The work was suspended after this first foundation subsidence. During this period, the Republic of Pisa was almost continually engaged in battles with Genoa, Lucca, and Florence, which allowed time for the underlying soil to settle.

About a century later, in 1272, construction was resumed under Giovanni di Simone and got as far as the sixth story. In an effort to compensate for the incline, the added floors were built out-plumb, by building one side higher than the other. However, construction was halted once again in 1284, when the Pisans were defeated by the Genoans in the battle of Meloria. The 7^{th} floor with the upper bell chamber was finally completed in 1319 by Tommaso, son of Andrea Pisano.

The ground underlying the Tower consists of three distinct layers. The first layer, called horizon A, is about 10 m thick and consists primarily of soft estuarine deposits of sandy and clayey silts laid down under tidal conditions. The second layer, called horizon B, consists of soft, normally consolidated marine clay, known as *Pancone* clay, which extends to a depth of about 40 m. This material is very sensitive and loses much of its strength if disturbed. The surface of the *Pancone* clay is dished beneath the Tower, revealing that the average subsidence is between 2.5 m and 3.0 m. The third layer, called horizon B, is dense sand which extends to considerable depth.

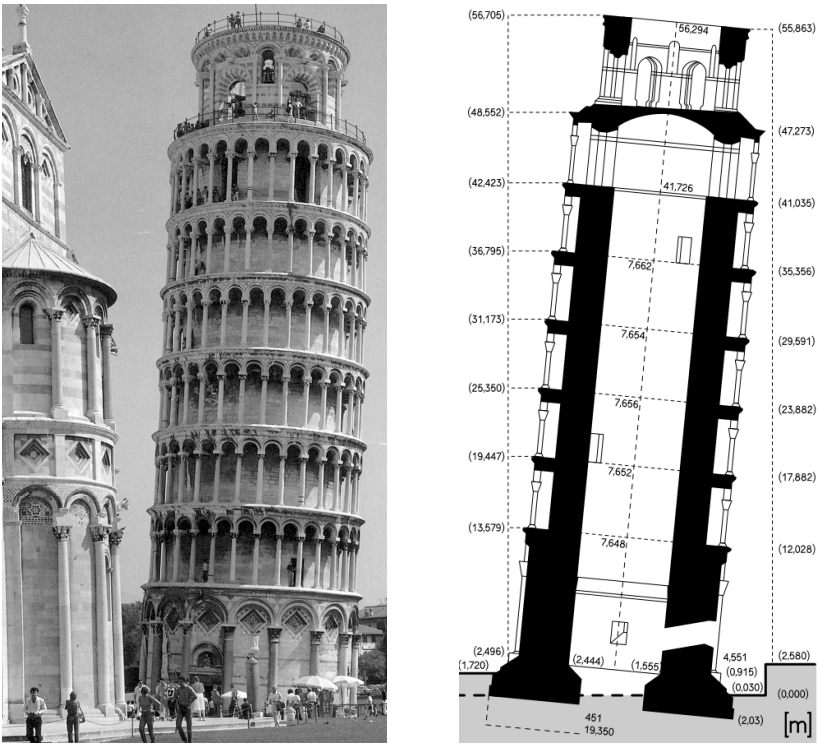

Fig. 7.53. The Leaning Tower of Pisa (From Wikipedia, Creative Commons, 2009)

The water table lies between 1 m and 2 m below the ground surface in horizon A. The continuous long-term tilting of the Tower could be explained by continuous variation of the water-table level that produced, by racketing, incremental plastic deformation of the solid structure of the soil. The soil subsided considerably and the high deformability of the Tower foundation may, on the contrary, be mainly due to the high compressibility of the *Pancone* Clay (Burland, 1998,1999).

By 1992 the tower was leaning by an angle of about 5.5 degrees toward the south. Precise measurements (begun in 1911) showed that during the 20th century the inclination of the Tower was increasing inexorably each year and the rate of tilting had doubled since the mid-1930s. In 1990 the tilting rate was about 6 arc-seconds per year, equivalent to a horizontal movement of about 1.5 mm per year at the top.

The diagram in figure 7.54 shows the history of the tower's rotation according to Burland (1998). The acceleration in the tilting from the year 1272–1360 has been attributed to soil consolidation during the first suspension of its construction.

Another considerable increase in rotation occurred in 1838, when A. Della Gherardesca excavated a walkway around the foundations, the so-called "*catino*", to facilitate access to the tower. This work resulted in an inrush of water on the south side, since the excavation here reached below the water table, and eventually in a increase in the tower's inclination of more than half a degree.

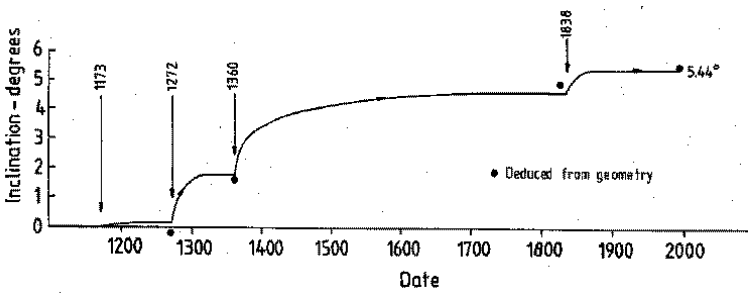

Fig. 7.54. Tower rotation in time (from Burland, 1998)

Crucial operations to stabilize the tower through sub-excavations were performed in the years 2000 – 2001, as shown in figure 7.54 (Jamalkowski, Burland, Viggiani 2003).

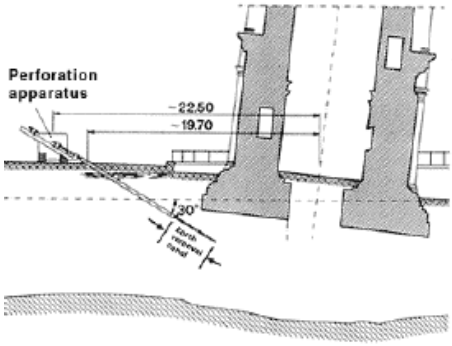

Fig. 7.55. Inclined drill for soil extraction (Burland, 1998)

The sub-excavation technique involved gradual removal of small quantities of soil from the side opposite the incline. This technique, engineered by Terracina (1962), had first been applied successfully to stabilize the cathedral of Mexico City (Tamez, Ovando, Santoyo, 1997). A large number of corkscrew drills were inserted at a shallow angle into the earth beneath the tower to remove soil from beneath the raised side of the tower. The progressive rotation was arrested, and the

tower was straightened by 45 cm to about four meters off-center - returnng it to its position in 1838.

Experimental research carried out at the Imperial College of London (Edmunds, 1993) has shown that the sub-excavation technique is strongly influenced by the extension and localization of the region of sub-excavated soil. It is interesting to point out that this study envisaged the existence of a critical depth for the region sub-excavated on the side opposite the inclination. The incline of the tower would actually worsen if the soil extraction were to continue beyond this depth, though the reasons for this seem to be not yet clear (Como, Ianniruberto and Imbimbo, 2001).

Some Technical Data on the Tower of Pisa

Weight (Lancellotta, 1993, Desideri, Russo and Viggiani, 1997): G = 14450 t.

Tilt of the tower prior to the stabilization operations, θ=5°, 40'.

Height of the tower center of mass with reference to the foundation: H_G = 22,515 m.

Initial tower inclination upon its completion: θ_{0i} = 0° 40' =0°.667 = 0.0116 rad. This value has been determined by evaluating the axis corrections attempted during the last stage of its construction. The tower, in fact, has a slightly curved 'banana' shape due to the addition of the last stories out-plumb, but at an angle to the lower stories, in an attempt to correct the tilting caused by settling of the foundation soil.

The ultimate resistant moment of the foundation and the initial rotational stiffness, according to Lancellotta, (1993): M_R = 60,000 tm; $K_{\theta 0}$ = 550,000 tm/rad.

Critical Weight Evaluation According to (104).

We shall now apply the foregoing formulations of the foundation resistant moment and the initial rotational stiffness, as drawn from Lancellotta (1993), to evaluate the critical weight of the tower.

Using the given values of $K_{\theta 0}$ and M_R, we calculate the factor γ_{oR}., which from (90), gives us: γ_{oR} = 0.109. The critical weight of the tower, corresponding to the its initial vertical position, from (105), is: $G_{cr.o}$ = 24,428 t.

We shall consider an initial inclination due to subsidence (according to Lancellotta) of θ_{oi} = 0°40' = 0.0116 rad, and from Eq. (100), the subsequent inclination due to foundation deformation is about θ^* = 0.050 rad = 2°,882'.

Thus, from Eq. (104), the critical weight of the tower turns out to be G^*_{cr} = 15472 t. The corresponding critical rotation of the tower would be $\theta_{oi} + \theta^*$ = 0°40' + 2°,882' = 3°,55', less than 5.5° measured before the recent stabilization work.

Let us now assume the following values for the ultimate moment and the initial foundation stiffness: M_R = 90,000 tm; $K_{\theta 0}$ = 500,000 tm/rad, together with a somewhat larger value of the initial inclination: θ_{oi} = 0°50' = 0°,83' = 0.015 rad.

From (90), we get γ_{oR} = 0.180 and from (103), $G_{cr.o}$ = 22,207 t. By applying Eq. (100), the tilting of the tower after the initial settlement turns out to be

θ^* = 0.073 rad = 4°,21'. The corresponding critical weight is lower, that is, G^*_{cr} = 14,863 t, only slightly larger than the tower's actual weight. The total inclination of the tower becomes 4°,21'+0°,83' = 5°,04', not too different from the rotation detected before its stabilization. Finally, the *safety factor*, evaluated in terms of the ratio between the critical and the actual weight of the tower, is very low, only about 14863/14450 = 1.03. Further studies could take into account the creep deformations of the soil. These evaluations, albeit approximate, reveal the precariousness of the tower's state back in 1990 and moreover highlight the relevance of the stabilization works carried out .

Appendix

A.6.1 Yokel Integration of the Differential Equation for the Flexure of a Eccentrically Loaded Cracked Pier

By means of Eq. (15), we obtain

$$\frac{d}{dx}\left(\frac{dy}{dx}\right)^2 = \frac{2dy}{dx}\cdot\frac{d^2y}{dx^2} = \frac{2k_1}{\left(u_0+y\right)^2}\cdot\frac{dy}{dx}$$

and

$$\left(\frac{dy}{dx}\right)^2 = 2k_1\int\frac{dy}{(u_0+y)^2} = -2k_1\frac{1}{u_0+y}+c_1 \quad .$$

For $y \to 0$, we have $dy/dx \to 0$ and consequently $c_1 = 2k_1/u_0$, and

$$\left(\frac{dy}{dx}\right)^2 = 2k_1\left(\frac{1}{u_0}-\frac{1}{u_0+y}\right) = \frac{2k_1}{u_0}\cdot\frac{y}{u_0+y} \quad ,$$

hence

$$\frac{dy}{dx} = \pm\sqrt{\frac{2k_1}{u_0}}\cdot\left(\frac{y}{u_0+y}\right)^{1/2} \quad . \tag{A1}$$

With the position

$$k_2 = \sqrt{\frac{2k_1}{u_0}} = \frac{2}{3}\sqrt{\frac{P}{Ebu_0}} \quad , \tag{A2}$$

equation (A1) becomes:

$$\frac{dy}{dx} = \pm k_2 \left(\frac{y}{u_0 + y}\right)^{1/2}$$

or

$$dx = \pm \frac{1}{k_2} \left(\frac{u_0 + y}{y}\right)^{1/2} \cdot dy \,.$$

Integration yields

$$x = \pm \frac{1}{k_2} \int \left(\frac{u_0 + y}{y}\right)^{1/2} dy$$

and, consequently

$$\int \left(\frac{u_0 + y}{y}\right)^{1/2} dy = \sqrt{y\left(u_0 + y\right)} + \frac{u_0}{2} \int \frac{dy}{\sqrt{y\left(u_0 + y\right)}} = \sqrt{y\left(u_0 + y\right)} + u_0 \ln\left(\sqrt{y} + \sqrt{u_0 + y}\right),$$

hence

$$x = \pm \frac{1}{k_2} \left[\sqrt{y\left(u_0 + y\right)} + u_0 \ln\left(\sqrt{y} + \sqrt{u_0 + y}\right)\right] + c_2 \,.$$

By applying boundary condition (15) (i.e., by accounting for the fact that at $x = 0$, $y = 0$), we get:

$$c_2 = -\frac{u_0}{k_2} \ln \sqrt{u_0}$$

and

$$x = \pm \frac{1}{k_2} \left[\sqrt{y\left(u_0 + y\right)} + u_0 \ln \frac{\sqrt{y} + \sqrt{u_0 + y}}{\sqrt{u_0}}\right] \,. \tag{A3}$$

Substituting (A3) into (A2) of k_2 furnishes:

$$x = \pm \frac{3}{2} \sqrt{\frac{Eb u_0}{P}} \cdot \left[\sqrt{y\left(u_0 + y\right)} + u_0 \ln \frac{\sqrt{y} + \sqrt{u_0 + y}}{\sqrt{u_0}}\right] \,.$$

By considering that for $x = h/2$, $y = u_1 - u_0$, the solution is expressed in terms of u_1:

$$\frac{h}{2} = \pm\frac{3}{2}\sqrt{\frac{Eb u_0}{P}} \cdot [\sqrt{u_1\left(u_1 - u_0\right)} + u_0 \ln\sqrt{\frac{u_1 - u_0}{u_0}} + \sqrt{\frac{u_1}{u_0}}] \ ,$$

and hence

$$P = \frac{9Eb u_0}{h^2} \cdot [\sqrt{u_1\left(u_1 - u_0\right)} + u_0 \ln(\sqrt{\frac{u_1 - u_0}{u_0}} + \sqrt{\frac{u_1}{u_0}})]^2 \ .$$

With the position

$$\alpha = u_0 / u_1 \ , \tag{A4}$$

we finally arrive at

$$P = \frac{9Eb u_1^3}{h^2} \cdot \alpha \cdot [\sqrt{1-\alpha} + \alpha \ln(\sqrt{\frac{1-\alpha}{\alpha}} + \sqrt{\frac{1}{\alpha}})]^2 \ . \tag{A5}$$

References

Burland, J.B.: The enigma of the leaning of the tower of Pisa. The sixth Spencer J. Buchanam Lecture. A&M University, Texas (December 9, 1998)

Burland, J.B., Jamiolkowski, M., Viggiani, C.: The Restoration of the Leaning Tower of Pisa: Geotechnical Aspects. In: Workshop on the Restoration of the Leaning Tower of Pisa, Preprint vol. 1, Pisa (1999)

Cervenka, V., Cervenka, J.: Atena program documentation, User's manual for Atena 2D, Prague (2002)

Como, M.: Plastic and Visco–Plastic Stability of Leaning Towers. In: Ferrarese, G., d'Elba, I. (eds.) Fisica matematica e Ingegneria: rapporti e compatibilità, Conv. Intern. in memoria di G. Krall, Pitagora, Bologna, Giugno 10-14 (1993)

Como, M., Ianniruberto, U.: Sulla resistenza laterale di pilastri caricati assialmente e costituiti da materiale elastico–non resistente a trazione. In: XII Congresso Naz. AIMETA 1995, Naples, Ottobre 3-6 (1995)

Como, M.T.: Il Restauro dei Monumenti a Torre in muratura. In: Restauro, pp. 152–153. Edizioni Scientifiche Italiane, Naples (2000)

Como, M., Ianniruberto, U., Imbimbo, M.: A rigid plastic model of the under–excavation technique applied to stabilize leaning towers. In: Lourenço, P.B., Roca, P. (eds.) Constructions, Guimarães (2001)

De Falco, A., Lucchesi, M.: Stability of no-tension beam–columns with bounded compressive strength. In: Proc. IASS–IACM 2000, Fourth Int. Colloq. Comput. Shell Spatial Struct., Chania Crete, Greece, June 4-7 (2000)

De Falco, A., Lucchesi, M.: Explicit solutions for the stability of no–tension beam–columns. Intern. Journ. of Struct. Stability and Dynamics 3(2), 195–213 (2003)

De Fez, A.: Il consolidamento degli edifici, Liguori, Naples (1992)

Desideri, A., Russo, G., Viggiani, C.: La stabilità di torri su terreno deformabile. Rivista Italiana di Geotecnica 1/97 (1997)

de Witte, F.C., Kikstra, W.P.: Diana User's Manual, Nonlinear Analysis. Delft, Netherlands (1990)

Edmunds, H.E.: The Use of Underexcavation as a means of Stabilising the Leaning Tower of Pisa: Scale and Model Tests. MSc thesis, Department of Civil Engineering, Imperial College of Science, Technology and Medicine, London (1993)

Frisch-Fay, R.: Stability of masonry piers. Int. Journal of Solids and Structures 11(2) (1975)

Giuffrè, A.: Letture sulla Meccanica delle Murature Storiche, Facoltà di Architettura dell'università di Roma La Sapienza, Rome (1990)

Krall, G.: Statica dei mezzi elastici cosiddetti viscosi e sue applicazioni. Acc. Naz.le dei Lincei, fasc. 3–4, Rome (1947)

Hambly, E.C.: Soil buckling and the leaning instability of tall structures. The Structural Engineer 63A(3) (1985)

Jamiolkowski, M., Burland, J.B., Viggiani, C.: The statbilisation of the leaning Tower of Pisa. Soil and Foundations 43(5) (2003)

La Mendola, L., Papia, M.: Stability of masonry piers under their own weight and eccentric load. Journ. of Struct. Engineering 119(6) (1993)

Lancellotta, R.: The stability of a rigid column with non–linear restraint. Geotechnique 2 (1993)

Meyerhof, G.G.: The ultimate bearing capacity of Foundations. Geotechnique 2(3) (1951)

Napoli, P.: Modellazione numerica della interazione struttura suolo. Atti del Dpt. di Ingegn. Strutturale, Politecnico di Turin (1992)

Norme Tecniche sulle Costruzioni, Ministero delle Infrastrutture e dei Trasporti (2005)

Shrive, N.G., England, G.L.: Elastic, creep and shrinkage behavior of masonry. Intern. Journ. of Masonry Construction 1(3) (1981)

Tamez, E., Ovando, E., Santoyo, E.: Underexcavation of Mexico City's Metropolitan Cathedral and Sagrario Church. In: Proc. 14th Int Conf. Soil Mech. & Foundtn. Engrg., vol. 4 (1997)

Terracina, F.: Foundations of the Tower of Pisa. Geotechnique 12, 4 (1962)

Yokel, F.Y.: Stability and load capacity of members with no tensile strength. Proc. A.S.C.E. 87, ST7 (1971)